

We are IntechOpen, the world's leading publisher of Open Access books Built by scientists, for scientists

6,900

Open access books available

186,000

International authors and editors

200M

Downloads

Our authors are among the

154

Countries delivered to

TOP 1%

most cited scientists

12.2%

Contributors from top 500 universities



WEB OF SCIENCE™

Selection of our books indexed in the Book Citation Index
in Web of Science™ Core Collection (BKCI)

Interested in publishing with us?
Contact book.department@intechopen.com

Numbers displayed above are based on latest data collected.
For more information visit www.intechopen.com



Terahertz Electromagnetic Waves from Semiconductor Epitaxial Layer Structures: Small Energy Phenomena with a Large Amount of Information

Hideo Takeuchi

*Department of Electronic Systems Engineering, School of Engineering,
The University of Shiga Prefecture
Japan*

1. Introduction

Terahertz electromagnetic waves have a frequency range between infrared light and microwaves: the frequency of 1 THz corresponds to the photon energy of 4.1 meV (33 cm^{-1}) and to the wavelength of $300\text{ }\mu\text{m}$. It is well known that the terahertz waves have a high sensitivity to the water concentration in materials. For example, Hu and Nuss compared the terahertz-wave transmittance image of the freshly cut leaf with that of the same leaf after 48 hours (Hu & Nuss, 1995). They demonstrated the freshness between the two leaves can be clearly evaluated from the terahertz-wave transmittance images. In addition, the terahertz waves are sensitive to explosive chemical materials (Yamamoto et al., 2004). Accordingly, the terahertz waves are applicable to a security system in airports because conventional x-ray inspection systems are insensitive to chemical materials. The above-mentioned characteristics of the terahertz wave lead to the reason why terahertz-wave spectroscopy is attractive. We note that the terahertz waves are useful to investigate the vibration of biological molecules, dielectric constant of materials, and so on (Nishizawa et al., 2005).

In the present chapter, we focus our attention on the time-domain terahertz-wave measurements based on the femtosecond-pulse-laser technology. Most of the terahertz-wave measurement systems employ photoconductive antenna devices (Auston, 1975; Nuss & Orenstein, 1999) as an emitter of terahertz waves. As mentioned later, the antenna-based terahertz emitters, which are categorized into a lateral/planer structure type emitter, have various disadvantages. For the progress in terahertz-wave spectroscopy, it is still required to develop convenient terahertz-wave emitters. Compound semiconductors with a surface electric field, by being irradiated by femtosecond-laser pulses, emit the terahertz wave originating from the surge current of the photogenerated carriers flowing from the surface to the internal side in the surface depletion layer. This phenomenon provides us a convenient terahertz emitter free from a device fabrication for an external applied bias. In the above terahertz emission mechanism, the doping concentration is a major factor determining the depletion-layer width and surface electric field, which are in the relation of trade-off. In order to obtain intense terahertz wave emission, earlier works focused on

searching a suitable compound semiconductor and subsequently adjusted the doping concentration (Gu & Tani, 2005). Moreover, external magnetic fields, which are of the order of 1 T, were used for enhancing the terahertz emission (Sarukura et al., 1998; Ohtake et al., 2005); however, the terahertz spectroscopic system with use of the magnetic field generator lacks the advantage of being convenient. In the above-mentioned earlier studies, bulk crystals were employed as emitters. From the viewpoint of utilizing the advantage of compound semiconductors, it should be emphasized that compound semiconductors are rich in a degree of freedom in designing their structures with use of the technology for epitaxial layer growth. Accordingly, we have focused our attention on the epitaxial layer structure, and have explored the feasibility of controlling characteristics of the terahertz waves by appropriately designing an epitaxial layer structure.

The purpose of the present chapter is to demonstrate the fact that the appropriate design of epitaxial layer structures is effective to control the characteristics of the terahertz wave. The above-mentioned epitaxial layer structure design is based on the fundamental semiconductor physics, so that the results demonstrated here contain a large amount of information on ultrafast carrier dynamics. We organize the present chapter based on our recent works (Takeuchi et al., 2008; 2009; 2010). In Section 2, we review the current status of terahertz-wave spectroscopy, and discuss the hidden problems. In Section 3, we approach the enhancement of the terahertz-wave emission using the way different from those of the earlier works; namely, we explore the feasibility of enhancing the terahertz-emission intensity by appropriately designing an epitaxial layer structure. We demonstrate that an undoped GaAs/*n*-type GaAs (*i*-GaAs/*n*-GaAs) epitaxial layer structure is effective to enhance the terahertz emission and that the emission intensity from the *i*-GaAs/*n*-GaAs sample can exceed the emission intensity from *i*-InAs that is known as one of the most intense terahertz emitters. In Section 4, we demonstrate frequency tunable terahertz emitters based on *i*-GaAs/*n*-GaAs epitaxial layer structures with various *i*-GaAs-layer thicknesses *d*, using the sub-picosecond-range carrier-transport processes. The observed time-domain terahertz waveform consists of the following two components: the intense monocycle oscillation, the so-called first burst, around the time delay of 0 ps originating from the surge current and oscillation patterns from the coherent GaAs longitudinal optical (LO) phonon. From the Fourier power spectrum of the terahertz waveform, it is elucidated that the enhancement of the built-in electric field in the *i*-GaAs layer, which is controlled by changing *d*, causes a high frequency shift of the first burst band. Based on the above-mentioned phenomenon, we discuss the photogenerated carrier transport in the sub-picosecond range. We also find that the intensity of the coherent LO phonon band increases with a decrease in *d*.

In the research field of terahertz waves, most of the efforts have been focused on how to enhance the terahertz intensity of emitters or on how to improve the quality of the terahertz-wave images, which indicates that the terahertz wave has been attracting attention only as a tool for probing a given sample under test. On the other hand, we emphasize that the terahertz waves contain a lot of information on physics of the terahertz-wave sources, which is also pointed out in Section 4. In Section 5, we especially focus our attention on this viewpoint, and investigate the direction of the surface band bending using terahertz-wave measurements. We utilize the polarity of the terahertz wave. We investigate the polarity of the terahertz wave from GaAs-based dilute nitride ($\text{GaAs}_{1-x}\text{N}_x$ and $\text{In}_y\text{Ga}_{1-y}\text{As}_{1-x}\text{N}_x$) epitaxial layers in order to clarify the effects of nitrogen incorporation on the direction of the surface band bending. The *i*-GaAs/*n*-GaAs sample has an upward band bending at the surface

region, which indicates that photogenerated electrons flow into the inside. In the $\text{GaAs}_{1-x}\text{N}_x$ samples, the terahertz-wave polarity is reversed; namely, the $\text{GaAs}_{1-x}\text{N}_x$ sample has a downward band bending. The reversal of the terahertz-wave polarity is attributed to the phenomenon that the conduction band bottom is considerably lowered by the band anticrossing peculiar to $\text{GaAs}_{1-x}\text{N}_x$, which results in approaching the conduction band bottom to the surface Fermi level. This modifies the direction of the surface band bending connected with the polarity of the terahertz wave. We also investigate the terahertz wave from an $\text{In}_y\text{Ga}_{1-y}\text{As}_{1-x}\text{N}_x$ epitaxial layer. It is found that the terahertz-wave polarity is also reversed in the $\text{In}_y\text{Ga}_{1-y}\text{As}_{1-x}\text{N}_x$ sample. Thus, we conclude that the direction reversal of the surface potential bending induced by the band anticrossing is universal in GaAs-based dilute nitrides.

Finally, we summarize this chapter and point out what should be elucidated next for the progress in terahertz-wave spectroscopy.

2. Problems hidden in current terahertz-wave spectroscopic measurements with use of photoconductive antenna devices

Recently, terahertz-wave spectroscopy shifts from the research stage to the commercial stage: terahertz-wave spectroscopic systems, which employ the femtosecond-pulse-laser technology, are commercially available. Most of the terahertz-wave measurement systems equip with a photoconductive antenna (Auston, 1975; Nuss & Orenstein, 1999) as a terahertz-wave emitter. Figures 1(a) and 1(b) show a typical bow-tie antenna and dipole antenna, respectively. The metal electrodes of the antennas are formed on the low-temperature-grown GaAs epitaxial layer (Othonos 1998). The application of the low-temperature-grown GaAs epitaxial layer to the antenna was proposed by Gupta et al., 1991. The gap of the antenna is about 5 μm . The generation mechanism of the terahertz wave is schematically shown in Fig. 1(c). The illumination of the laser pulses (the pump beam) induces the surge current of the photogenerated carriers j . According to Faraday’s law of induction, the electric field of the terahertz wave $E_{\text{THz}}(t)$ is expressed by the following equation (Bolivar, 1999):

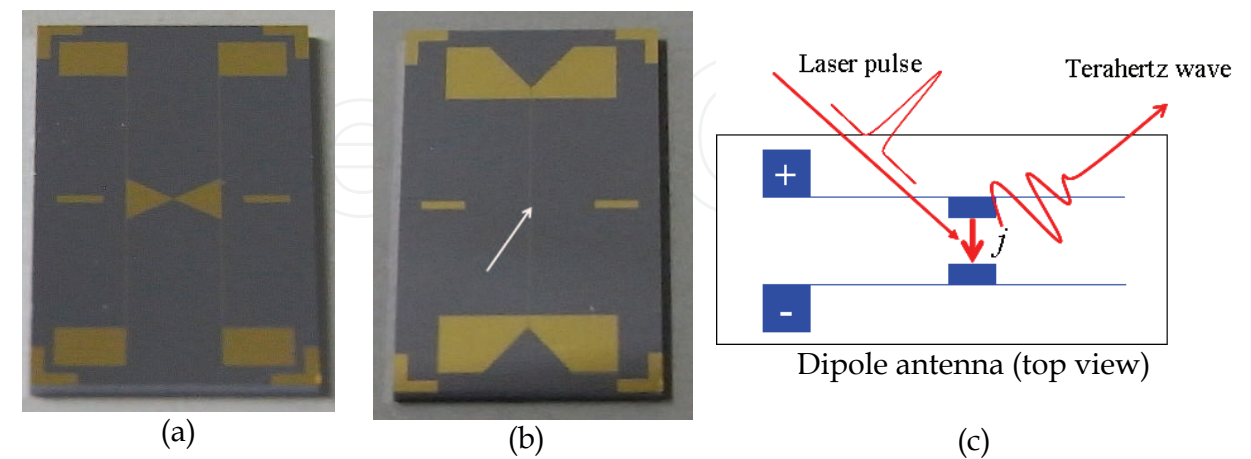


Fig. 1. (a) Optical photograph of a bow-tie antenna. The gap between the triangles is the area emitting the terahertz wave. (b) Optical photograph of a dipole antenna. The position of the arrow corresponds to the gap area emitting terahertz wave. (c) Generation mechanism of the terahertz wave in the dipole antenna under the external bias voltage.

$$E_{\text{THz}}(t) \propto \frac{\partial}{\partial t} j(t) \quad (1)$$

Equation (1) is a basic relation between the surge current and terahertz wave. In addition, it should be mentioned that the emission of the terahertz wave occurs in the reflection and transmission directions of the pump beam. The emission of the terahertz wave along the reflection direction is expressed with use of the generalized Fresnel equation (Bolivar, 1999):

$$n_{\text{pump}}^{\text{air}} \sin(\theta_{\text{pump}}^{\text{air}}) = n_{\text{terahertz}}^{\text{air}} \sin(\theta_{\text{terahertz}}^{\text{air}}) \quad (2)$$

Here, $n(\omega_{\text{pump}}^{\text{air}})$ and $n(\omega_{\text{terahertz}}^{\text{air}})$ are the refractive indices of the pump beam and of the terahertz wave, respectively. The quantities of $\theta_{\text{pump}}^{\text{air}}$ and $\theta_{\text{terahertz}}^{\text{air}}$ denote the angle of incidence of the pump beam and the emission angle of the terahertz wave, respectively. In general, the refractive index of the pump beam can be approximated to that of the terahertz wave. Accordingly, the emission direction of the terahertz wave is almost the same as the reflection direction of the pump beam.

As mentioned above, the photoconductive antennas are usually used for the terahertz-wave measurement; however, the antennas are fragile and less controllable. The one factor originates from the narrow gap of the antenna placed on the surface, which is weak against the static electricity. Another factor arises from the fact that the low-temperature-grown GaAs epitaxial layer is unstable in principle. Furthermore, the transport process of the photogenerated carriers is remarkably sensitive to the growth condition of the epitaxial layer (Abe et al., 1996; Othonos, 1998). We also point out the disadvantage that the lateral carrier transport along the surface is influenced by the surface degradation arising from humidity and oxidation. These problems of the planer photoconductive antennas lead to the reason why the terahertz emitters with use of the vertical carrier transport are attractive.

3. Intense terahertz emission from an *i*-GaAs/*n*-GaAs structure

3.1 Terahertz waves from the bulk crystals of compound semiconductors

In advance to describing the terahertz emission from the *i*-GaAs/*n*-GaAs structure, we briefly describe the terahertz wave from bulk crystals.

Figures 2(a) and 2(b) schematically show the generation mechanism of the terahertz wave in the bulk crystal. In general, as shown in Fig. 2(a), compound semiconductors have a surface band bending, which results from the surface Fermi level pinning owing to the presence of the surface states (Aspnes, 1983; Wieder, 1983). The band bending forms a built-in electric field and surface depletion layer. In the case where the photon energy of the pump beam is larger than the band-gap energy, the real excitation of carriers occurs. The photogenerated carriers are accelerated by the built-in electric field, which leads to the drift motion and to the generation of the surge current j . The surge current is the source of the terahertz wave, as expressed by Eq. (1). The terahertz wave is, according to Eq. (2), emitted in the same direction as that of the reflected pump beam, as shown in Fig. 2(b). We also note that the other generation mechanism of the surge current exists: the photo-Dember effect induced by the carrier diffusion dominating in narrow gap semiconductors such as InAs. In GaAs, the drift motion is dominant because, even in the presence of the negligibly low electric field (several kV/cm), the photo-Dember effect is quite small owing to the slight excess energy

(Heyman et al., 2003). The photo-Dember effect is out of the scope of the present chapter. The details of the photo-Dember effect are described by Gu and Tani, 2005.

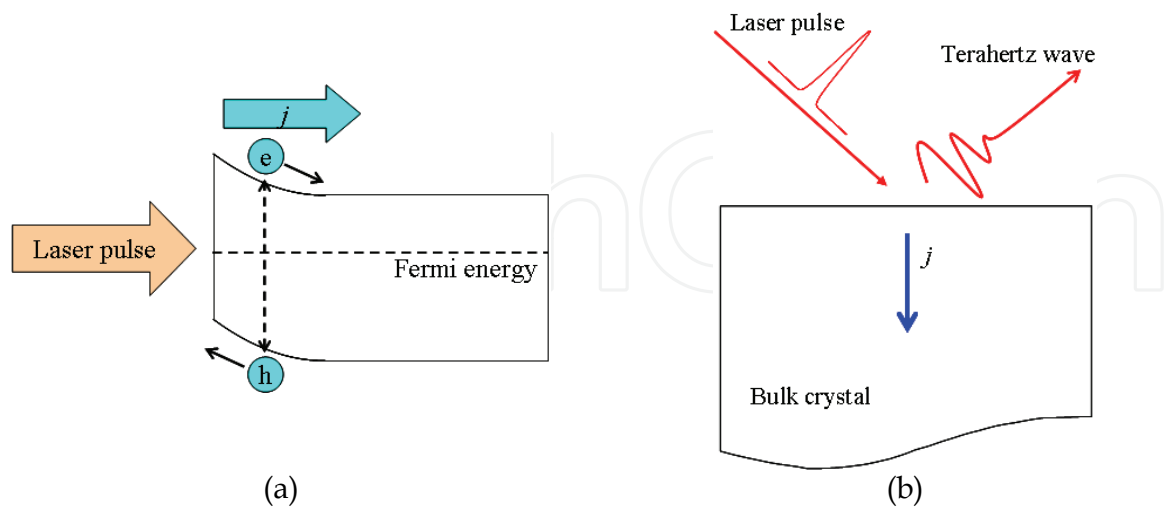


Fig. 2. (a) Band diagram of a semiconductor crystal. The surface Fermi level pinning causes the band bending and forms the surface depletion layer. (b) Generation mechanism of the terahertz wave. The flow of the photogenerated electrons (e) and holes (h) which are shown in Fig. 2(a), leads to the surge current j resulting in the emission of the terahertz wave.

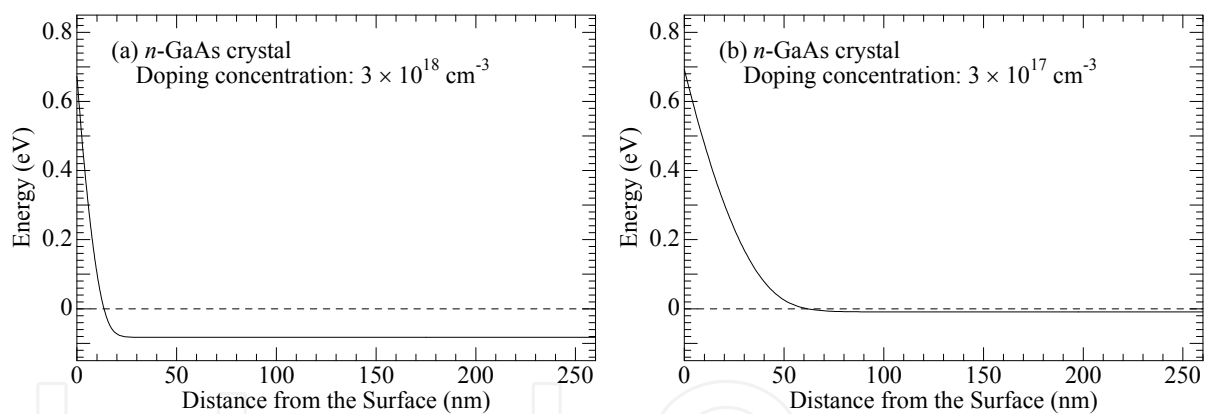


Fig. 3. Potential energies of the n -GaAs bulk crystals as a function of distance from the surface calculated on the basis of the Boltzmann-Poisson model. The solid lines indicate the conduction-band energy. The origin of the energy axis corresponds to the Fermi level, which is denoted as the dashed lines. (a) n -GaAs bulk crystal with a doping concentration of $3 \times 10^{18} \text{ cm}^{-3}$. (b) n -GaAs bulk crystal with a doping concentration of $3 \times 10^{17} \text{ cm}^{-3}$.

As mentioned above, the built-in electric field is a major factor dominating the surge current. It should be mentioned that the built-in electric field is in the trade-off with the thickness of the surface depletion layer. Figures 3(a) shows the potential energy of the n -GaAs crystal with a doping concentration of $3 \times 10^{18} \text{ cm}^{-3}$ as a function of distance from the surface calculated on the basis of the Boltzmann-Poisson model (Basore, 1990; Clugston & Basore, 1998). In the calculation, the parameters used are the same as those employed in our earlier work (Takeuchi et al., 2005). In addition, the effect of the band-gap shrinkage (Huang et al., 1990) is also taken into account. The solid and dashed lines are the conduction band

energy and Fermi energy, respectively. The pinning position of the surface Fermi level locates at the center of the band gap in GaAs (Shen et al., 1990). As shown in Fig. 3(a), the conduction-band energy remarkably bends around the surface owing to the surface Fermi-level pinning. The electric field at the surface is estimated to be 775 kV/cm, which is relatively large. The thickness of the surface depletion layer is, however, estimated to be about 10 nm at most; namely, the region for the surge current flow is quite limited. In contrast, as shown in Fig. 3(b), the thickness of the surface depletion layer is estimated to be about 60 nm in the *n*-GaAs crystal with a doping concentration of $3 \times 10^{17} \text{ cm}^{-3}$; however, the electric field at the surface is estimated to be 250 kV/cm. This value is much smaller than that in the *n*-GaAs crystal with a doping concentration of $3 \times 10^{18} \text{ cm}^{-3}$. From the above-mentioned discussion, it is apparent that the built-in electric field is actually in the trade-off with the thickness of the surface depletion layer. We also note that the depletion-layer thickness is much smaller than the penetration length of the typical femtosecond laser pulse with a center wave length of 800 nm: the value of the above-mentioned penetration depth is estimated to be about 740 nm (Madelung, 2004). This fact means that the photogenerated carrier density in the depletion layer is negligibly small in comparison with the photogenerated carrier density in the internal side (bulk crystal region). It is, therefore, conclude that the adjustment of the doping concentration of the bulk crystal is an inappropriate strategy for controlling the characteristics of the terahertz wave.

3.2 Design of the epitaxial layer structure: potential structure of the *i*-GaAs/*n*-GaAs structure

From the present subsection, we describe the main theme of the present chapter: terahertz electromagnetic waves from semiconductor epitaxial layer structures. Initially, we describe the strategy for designing the epitaxial layer structure on the basis of the potential structure. The calculated potential structure of the *i*-GaAs (200 nm)/*n*-GaAs ($3 \mu\text{m}$, $3 \times 10^{18} \text{ cm}^{-3}$) epitaxial layer structure is shown in Fig. 4, where the values in the parentheses denote the layer thickness and doping concentration. The conduction-band energy of the *i*-GaAs/*n*-GaAs structure, which is indicated by the solid line, has a linear potential slope in the whole

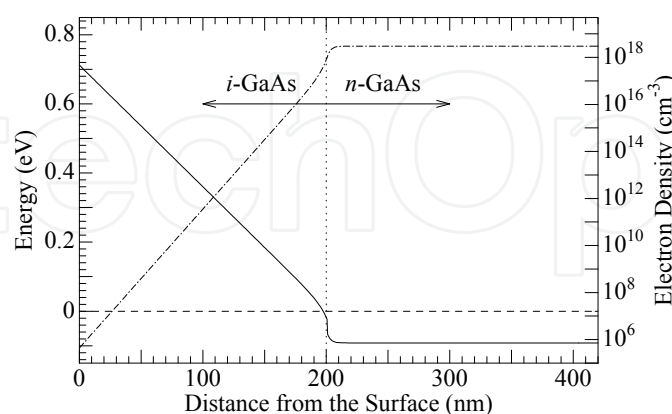


Fig. 4. Potential energy of the *i*-GaAs(200 nm)/*n*-GaAs ($3 \mu\text{m}$ $3 \times 10^{18} \text{ cm}^{-3}$) structure as a function of distance from the surface calculated on the basis of the Boltzmann-Poisson model. The solid and dashed lines indicate the conduction-band energy and Fermi level, respectively. The dashed-and-dotted line denotes the electron density in the *i*-GaAs/*n*-GaAs structure calculated as a function of distance from the surface.

i-GaAs layer with a thickness of 200 nm, which results from the fact that the *i*-GaAs top layer is free from dopants. The *i*-GaAs layer has a uniform built-in electric field of 35 kV/cm owing to the linear potential slope. Note that the *i*-GaAs layer thickness is much larger than the surface-depletion-layer thicknesses of the *n*-GaAs crystals shown in Figs. 3(a) and 3(b). Accordingly, the photogeneration of the carriers are more effective than those in *n*-GaAs crystals. We discuss in Subsection 3.4 and Section 4 the details whether the built-in electric field in the *i*-GaAs/*n*-GaAs sample is sufficient or not.

It should be pointed out that the *i*-GaAs/*n*-GaAs structure has another merit. The dashed-and-dotted line denotes the calculated electron density. The electron density in the *i*-GaAs layer is much smaller than that in the *n*-GaAs layer, which is advantageous for emitting intense terahertz wave because the terahertz wave is strongly absorbed by the free carriers (Nishizawa et al., 2005). From the above discussion, it is expected that the intense terahertz emission can be obtained with use of the *i*-GaAs/*n*-GaAs structure.

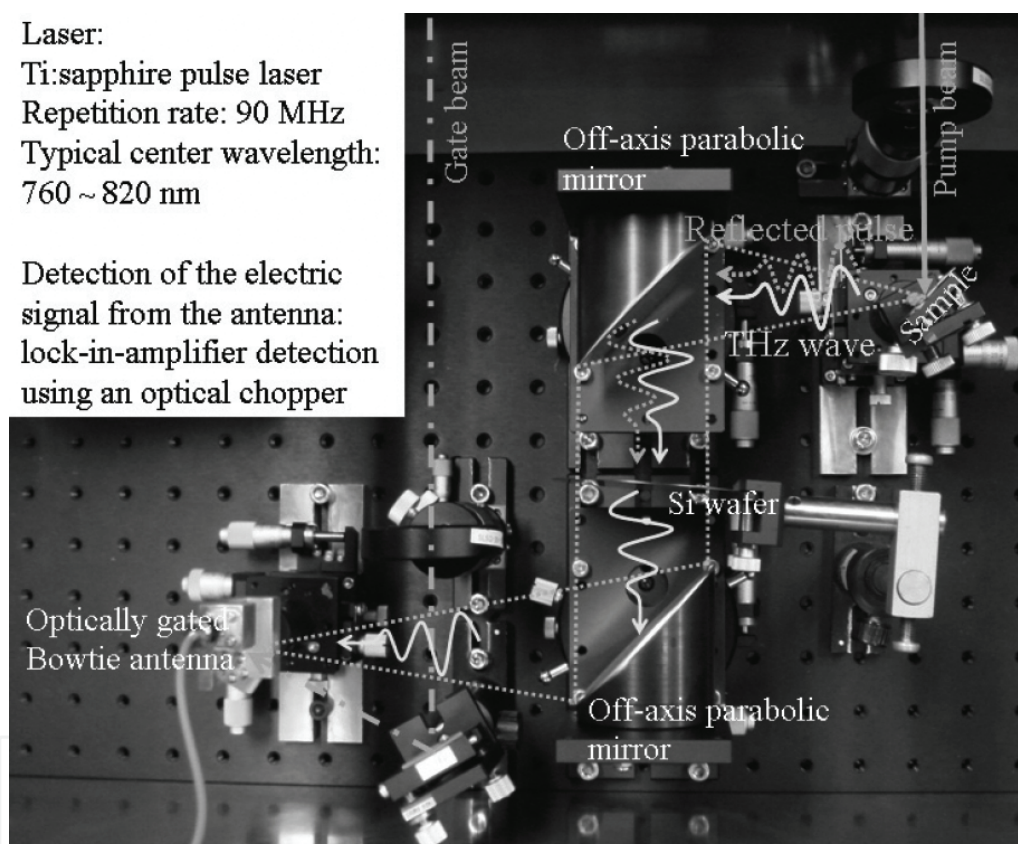


Fig. 5. Photograph of the layout of the optical components for the terahertz-wave measurement.

3.3 Samples and experimental procedure

The present sample was an *i*-GaAs (200 nm)/*n*-GaAs (3 μm , $3 \times 10^{18} \text{ cm}^{-3}$) structure grown on a 2°-off semi-insulating (001)-oriented GaAs substrate by metal organic vapour phase epitaxy, where the values in the parentheses denote the individual layer thickness and doping concentration.

The time-domain terahertz-wave signals from the samples were measured at room temperature with use of laser pulses with a duration time of about 70 fs. The measurement

system for the terahertz wave is shown in Fig. 5 as a photograph. The sample, by being illuminated by the pump beam, emits a terahertz wave along the reflection direction of the pump beam as described in Section 2. The emitted terahertz wave was collected with use of two off-axis parabolic mirrors. The high resistivity silicon wafer was placed as a filter for the pump beam. The collected terahertz wave was focused on the bow-tie antenna with a gap of $5.0\ \mu\text{m}$ formed on a low-temperature-grown GaAs. The bow-tie antenna was optically gated with use of the laser-pulse beam (gate beam), which was controlled by the mechanical delay line, the so-called stepper. Consequently, the terahertz wave was detected only in the case where the bow-tie antenna was illuminated by the gate beam. The above-mentioned method for the detection of the terahertz wave is the so-called optically gating technique (Nuss & Orenstein, 1999; Bolivar, 1999). In the present experiment, the power of the gate beam was fixed to 4.0 mW. For the reference samples, a (001) *n*-GaAs (about $2 \times 10^{18}\ \text{cm}^{-3}$) crystal and a (001) *i*-InAs crystal were examined.

3.4 Intense terahertz emission caused by the surge current in the *i*-GaAs/*n*-GaAs structure

Figure 6(a) shows the terahertz waveforms of the *i*-GaAs/*n*-GaAs (solid line), *n*-GaAs (dotted line), and *i*-InAs (dashed line) samples at the pump-beam energies of 1.531, 1.589, and 1.621 eV. All the samples show a monocycle oscillation around the time delay of 0 ps, the so-called first burst. It is obvious that the amplitude of the first-burst of the *i*-GaAs/*n*-GaAs sample is larger by a factor of 10 than that of the *n*-GaAs crystal. It should be emphasized that the *i*-GaAs/*n*-GaAs sample emits the more intense terahertz wave, in spite of the fact that the built-in electric field is much weaker than the surface electric fields of the *n*-GaAs crystals shown in Figs. 3(a) and 3(b). The above-mentioned results indicate that the presence of the relatively thick *i*-GaAs layer, which is depleted, actually leads to the enhancement of the emission intensity. Thus, it is concluded that the appropriate epitaxial layer structure plays an important role for enhancing the terahertz-emission intensity.

Next, we discuss the pump-beam energy dependence of the terahertz emission, comparing the first-burst amplitude of the *i*-GaAs/*n*-GaAs sample with that of the *i*-InAs crystal. The increase in the pump-beam energy corresponds to an increase in the absorption coefficient. The absorption coefficients of GaAs (InAs) at 1.531, 1.589, and 1.621 eV are 1.41×10^{-3} (6.95×10^{-3}), 1.77×10^{-3} (7.69×10^{-3}), and 1.96×10^{-3} (8.09×10^{-3}) nm^{-1} , respectively (Madelung 2004); namely, the increase in the pump-beam energy from 1.531 to 1.621 eV magnifies the absorption coefficient of GaAs (InAs) by 1.39 (1.16). In the present *i*-GaAs/*n*-GaAs sample, the penetration depth, which is the reciprocal of the absorption coefficient, is much longer than the *i*-GaAs layer thickness. Consequently, the increase in the absorption coefficient leads to the enhancement of the terahertz emission efficiency because the total carrier number accelerated in the *i*-GaAs layer increases. The absorption coefficients of InAs are relatively insensitive to the change in the photon energy because the fundamental transition energy of InAs (0.354 eV) is much smaller than that of GaAs (1.424 eV) (Madelung, 2004).

The effect of an increase in the absorption coefficient on the emission intensity clearly appears in Fig. 6(a). At 1.531 eV, the first-burst amplitude of the *i*-GaAs/*n*-GaAs sample is slightly smaller than that of the *i*-InAs crystal, while, at 1.589 and 1.621 eV, the first-burst amplitudes of the *i*-GaAs/*n*-GaAs sample are remarkably larger than those of the *i*-InAs crystal; namely, the first-burst amplitude of the *i*-GaAs/*n*-GaAs sample is enhanced by the increase in the photogenerated carriers. Thus, it is experimentally confirmed that the

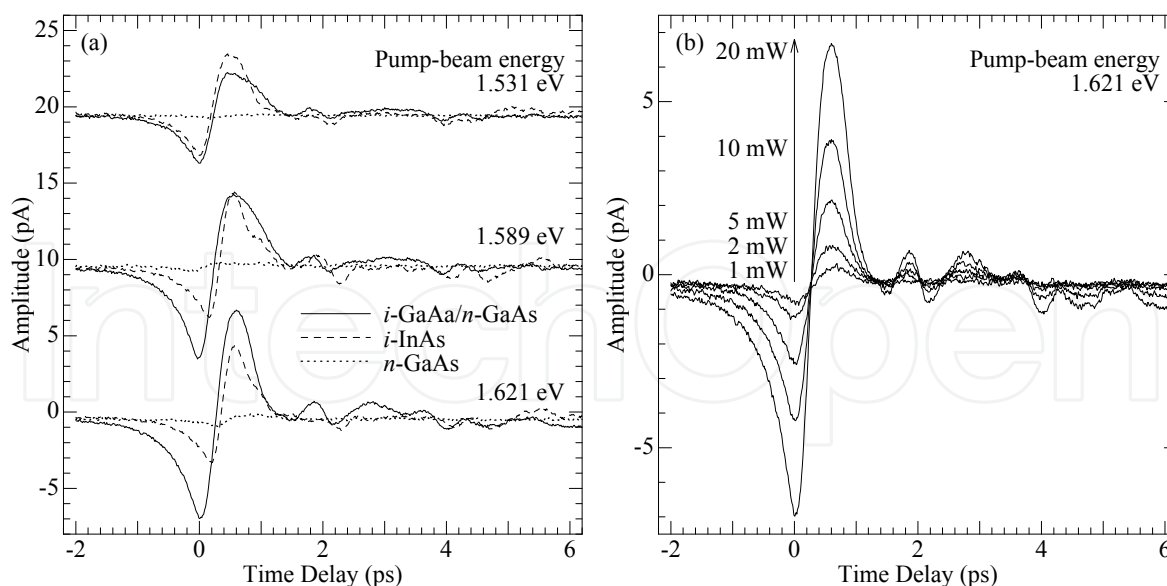


Fig. 6. (a) Amplitude of the terahertz waveform as a function of time delay at room temperature. The solid, dotted, and dashed lines indicate the time domain signals of the *i*-GaAs/*n*-GaAs, *n*-GaAs, and *i*-InAs samples, respectively. The pump-beam power was constant: 20 mW, while the pump-beam energies were varied: 1.531, 1.589, and 1.621 eV. For clarity, each waveform is vertically shifted. (b) Terahertz waveforms as a function of time delay in the *i*-GaAs/*n*-GaAs sample at the various pump-beam powers. The pump-beam energy was 1.621 eV.

dominant generation mechanism of the terahertz emission is attributed to the surge current of the photogenerated carriers flowing through the *i*-GaAs layer. It was reported that the terahertz emission intensity from GaAs is weaker by a factor of 10 than that of InAs (Ohtake et al., 2005). Taking this report into account, we conclude that the *i*-GaAs/*n*-GaAs structure is a solution for enhancing the terahertz emission intensity.

We also investigated the pump-beam-power dependence of the terahertz wave from the *i*-GaAs/*n*-GaAs structure. Figure 6(b) shows the terahertz waveforms of the *i*-GaAs/*n*-GaAs sample as a function of time delay at various pump-beam powers. The pump-beam energy was 1.621 eV. Except for the amplitude, all the waveforms have the same pattern. Taking account of the fact that the pattern of the waveform is a response from the surge current flowing in the *i*-GaAs layer, we conclude that the flow of the surge current does not depend on the pump-beam power in the *i*-GaAs/*n*-GaAs sample.

4. Frequency control of the terahertz waves using *i*-GaAs(*d* nm)/*n*-GaAs structures

4.1 Relation among the electric field, carrier-transport process, and terahertz wave

In section 3, we focused our attention on the terahertz wave from the *i*-GaAs (200 nm)/*n*-GaAs structure from the viewpoint of how to enhance the emission intensity. It is also worthy to investigate the characteristics of the terahertz waves from the *i*-GaAs(*d* nm)/*n*-GaAs structures with various *i*-GaAs layer thicknesses *d* because the *i*-GaAs(*d* nm)/*n*-GaAs structure has the ability to control the built-in electric field of the *i*-GaAs layer. The potential energies of the *i*-GaAs(200 nm)/*n*-GaAs structure and those of the *i*-GaAs(500 nm)/*n*-GaAs

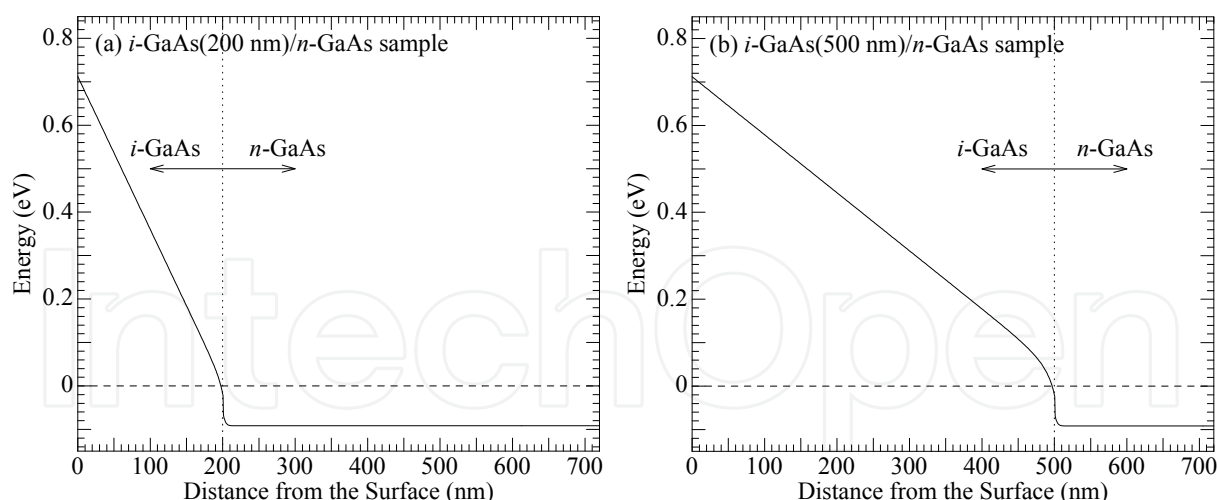


Fig. 7. Potential energy of the $i\text{-GaAs}(d \text{ nm})/n\text{-GaAs}$ structure as a function of distance from the surface calculated on the basis of the Boltzmann-Poisson model. The doping concentration and layer thickness of the $n\text{-GaAs}$ layer are $3 \times 10^{18} \text{ cm}^{-3}$ and $3 \mu\text{m}$, respectively. The solid and dashed lines indicate the conduction-band energy and Fermi level, respectively. (a) $d = 200 \text{ nm}$. (b) $d = 500 \text{ nm}$.

structure are depicted in Figs. 7(a) and 7(b), respectively, as a function of distance from the surface. Comparing Fig. 7(a) with Fig. 7(b), it is evident that the potential slope increases with a decrease in d , which means the built-in electric field in the $i\text{-GaAs}$ layer can be controlled by d . The values of the built-in electric field are calculated to be 35 and 13 kV/cm for the $i\text{-GaAs}(d \text{ nm})/n\text{-GaAs}$ samples with $d = 200$ and 500 nm , respectively.

From the viewpoint of semiconductor physics, the $i\text{-GaAs}(d \text{ nm})/n\text{-GaAs}$ structures are suitable for the investigation of the carrier-transport process in the presence of an electric field. In GaAs under the steady state condition, the electron drift velocity increases with an increase in an electric field and reaches the maximum velocity at the electric field of 4 kV/cm (Blakemore, 1982). Above 4 kV/cm, the electron velocity decreases in spite of an increase in an electric field and almost saturates at 10 kV/cm. The electron-velocity saturation is attributed to the effects of the intervalley scattering (Blakemore, 1982). The progress in the femtosecond-pulse-laser technology enables the transient photogeneration of carriers within the sub-picosecond range. This progress gives a chance to clarify whether the carrier-transport processes in the steady state are also valid in the sub-picosecond range. In order to investigate the carrier-transport process in sub-picosecond range, the terahertz-wave measurements are suitable because, as shown in Eq. (1), the electric field of the terahertz wave is proportional to the time derivative of the surge current of the photogenerated carriers; namely, the electric field of the terahertz wave is connected with the acceleration of the photogenerated carriers. Consequently, in the Fourier power spectrum of the terahertz waveform, the band originating from the surge current of the photogenerated carriers shifts to a high frequency side in the case where the photogenerated carriers are monotonously accelerated without being affected by the intervalley scattering. This theme is not only scientifically interesting but also technologically important because it leads to the realization of frequency tunable terahertz-wave emitters that enable the spectrally resolved time-domain terahertz measurement.

In Section 4, we explore the sub-picosecond-range carrier-transport processes in the *i*-GaAs (*d* nm)/*n*-GaAs structures with various *i*-GaAs-layer thicknesses *d* ranging from 200 to 2000 nm and present the realization of the frequency tunable terahertz-wave emitters. In addition, we discuss the intense terahertz emission from the coherent GaAs LO phonons, which leads to the monochromatic terahertz-wave source.

4.2 Confirmation of the controllability on the built-in electric field

The present samples were the *i*-GaAs (*d* nm)/*n*-GaAs structures grown on semi-insulating (001) GaAs substrates by metal organic vapour phase epitaxy. The layer thickness and doping concentration of the *n*-GaAs layer were 3 μm and $3 \times 10^{18} \text{ cm}^{-3}$, respectively. The values of *d* were 200, 500, 800, 1200, and 2000 nm. The sheet resistances of all the samples are the same value of 3.1 Ω per square, which indicates that the doping process was well controlled.

In the present experiment, it is essential to experimentally confirm the change in the built-in electric field. In order to estimate the built-in electric field, we applied the photorefectance measurement, which is a convenient and non-destructive method to estimate the built-in electric field. The details of the photorefectance measurements are described in the review paper by Pollak and Shen, 1993.

Figure 8(a) shows the photorefectance spectra of the *i*-GaAs(200 nm)/*n*-GaAs and *i*-GaAs(500 nm)/*n*-GaAs samples. In the photorefectance measurement, the pump beam was the laser light with a photon energy of 1.96 eV chopped at the frequency of 630 Hz. The pump-beam power was 2.0 mW. The probe beam was obtained from a tungsten-halogen lamp dispersed by a monochromator with a resolution of 0.5 nm. The probe-beam power was about 4 μW . As shown in Fig. 8(a), the oscillation patterns, the so-called Franz-Keldysh oscillations (FKOs), are observed. Since the FKOs are caused by an electric field, the appearance of the FKOs indicates the presence of the built-in electric field in the *i*-GaAs layer. In order to estimate the built-in electric field, as shown in Fig. 8(b), the extrema of the FKOs from the *i*-GaAs layer are plotted as a function of quasi-index $\xi \equiv [(3\pi/4) \cdot (j-1/2)]^{2/3}$, where *j* denotes the index of each extremum numbered from the fundamental transition energy position (Aspnes, 1974). The slope of the solid line is the electro-optic energy $\hbar\Theta$ given by $(e^2\hbar^2F^2/2\mu)^{1/3}$, where *F* and μ are the built-in electric field and interband reduced effective mass, respectively (Aspnes, 1974). From the slope of the solid line, it is evident that the built-in electric field of the *i*-GaAs(200 nm)/*n*-GaAs sample is higher than that of the *i*-GaAs(500 nm)/*n*-GaAs sample. It is, therefore, confirmed that the built-in electric field of the *i*-GaAs(*d* nm)/*n*-GaAs sample is enhanced by decreasing *d*. The built-in electric fields of the *i*-GaAs(*d* nm)/*n*-GaAs samples are estimated and listed in Table 1, using the relation of $\hbar\Theta \equiv (e^2\hbar^2F^2/2\mu)^{1/3}$. In this estimation of the built-in electric field, the used value of μ , which is the reduced effective mass of a GaAs bulk crystal, is 0.0556 in units of the electron rest mass m_0 in vacuum (Nelson et al., 1987). In Table 1, the results of the numerical calculation are also indicated. The estimated built-in electric fields are almost in good agreement with the calculated value, which means that the present samples are appropriately designed. Note that the built-in electric fields of the *i*-GaAs(*d* nm)/*n*-GaAs samples with *d* = 200 and 500 nm are in the range where the electron velocity saturates under the steady state condition.

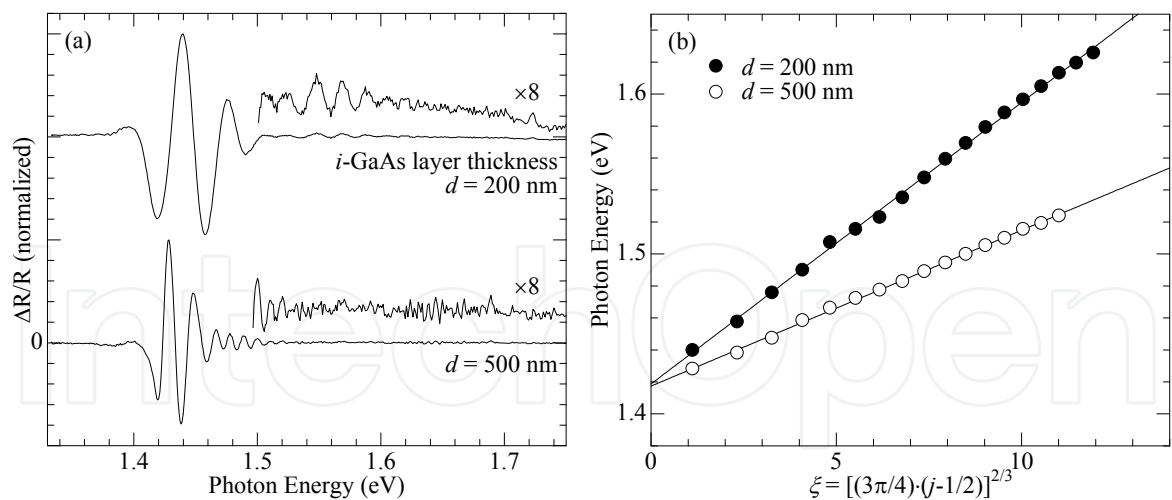


Fig. 8. (a) Photoreflectance spectra of the i -GaAs(200 nm)/ n -GaAs and i -GaAs(500 nm) / n -GaAs samples at room temperature. (b) Plots of the extrema of the FKOs from the i -GaAs(200 nm)/ n -GaAs sample (closed circles) and i -GaAs(500 nm)/ n -GaAs sample (open circles) as a function of quasi-index ξ .

Structure	F (kV/cm) ^{*1}	F (kV/cm) ^{*2}
i -GaAs(200 nm)/ n -GaAs	28	35
i -GaAs(500 nm)/ n -GaAs	12	13
i -GaAs(800 nm)/ n -GaAs	8.2	8.1
i -GaAs(1200 nm)/ n -GaAs	6.1	5.2
i -GaAs(2000 nm)/ n -GaAs	4.7	3.1

Table 1. Built-in Electric field F in the i -GaAs layer. *1: Estimated value from the electro-optic energy $\hbar\Theta$. *2: Calculated value on the basis of the Boltzmann-Poisson model.

4.3 Frequency tunability of the terahertz wave originating from the surge current

In the present terahertz-wave measurement, the experimental apparatus was almost the same as that described in Section 3, though there were some improvements. In the present experiment, we used a dipole antenna with a gap of 6.0 μm formed on a low-temperature-grown GaAs because the range of the frequency-dependent sensitivity of the dipole antenna is wider than that of the bow-tie antenna. In addition, to remove the effects of the water vapour absorption on the terahertz wave, the humidity was suppressed to be 10% during the measurement under a nitrogen-gas-purge condition. The powers of the pump and gate beams were fixed to 40 and 10 mW, respectively. The photon energies of the pump and gate beams were the same: 1.57 eV. The scan range of the time delay was from -2 to 8 ps. All the measurements were performed at room temperature.

The time-domain terahertz waveforms of the samples are shown in Fig. 9(a). All the samples exhibit an intense monocycle oscillation around the time delay of 0 ps, the so-called first burst resulting from the surge current of the photogenerated carriers. The amplitude of the first burst is relatively pronounced, which results from the fact that the i -GaAs layer of the i -GaAs(d nm)/ n -GaAs samples is depleted by its built-in electric field. Accordingly, the terahertz wave from the i -GaAs(d nm)/ n -GaAs structures provides the more precise information on the first burst related to the surge current.

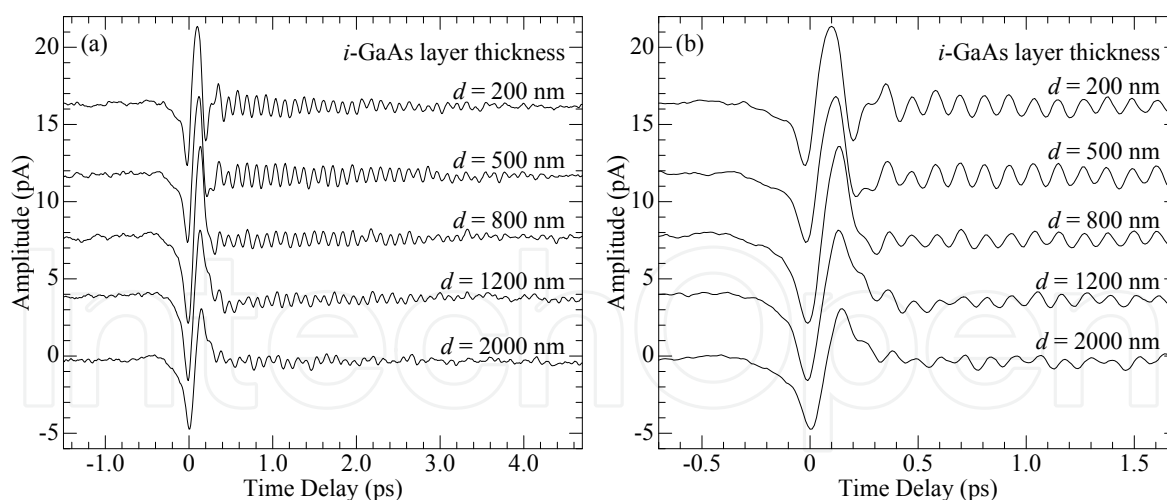


Fig. 9. (a) Amplitudes of the terahertz waveforms of the *i*-GaAs(d nm)/*n*-GaAs samples as a function of time delay at room temperature. The pump-beam power was fixed to be 40 mW. (b) Terahertz waveforms within the time delay from -0.5 to 1.5 ps.

The first burst shown in Fig. 9(a) is followed by an oscillatory profile with a period of 113 fs. The period corresponds to the frequency of the GaAs LO phonon (8.8 THz); namely, the terahertz emission from the coherent LO phonon is also detected. The details of terahertz emission from the coherent LO phonon are discussed in Subsection 4.5.

For the clarity of the shape of the first burst signal, Fig. 9(b) shows the first burst signal within the time delay from -0.5 to 1.5 ps. The amplitudes of the first burst signals are almost same in all samples, while the width of the first burst signal exhibits a gradual narrowing with a decrease in the *i*-GaAs layer thickness. Taking account of the fact that the decrease in the *i*-GaAs layer thickness results in the enhancement of the built-in electric field accelerating photogenerated carriers, the increase in the electron velocity, which corresponds to the enhancement of the surge current, has a tendency not to enhance of the amplitude of the first burst signal but to cause the change in the frequency components forming the first burst signal.

In order to analyze the frequency components, we transformed the terahertz waveforms to the Fourier power spectra, which are shown in Fig. 10(a). The Fourier power spectrum of each sample exhibits the two bands. Judging from the oscillation period in the time-domain signal shown in Fig. 9(a), the low frequency band is assigned to the band originating from the first burst. The band of the first burst gradually shifts to a high frequency side with a decrease in d . For example, the peak frequency of the first burst band locates at 1.5 THz in the *i*-GaAs(2000 nm)/*n*-GaAs sample, while the peak frequency of the first burst band locates at 4.0 THz in the *i*-GaAs(200 nm)/*n*-GaAs sample. This is the significant finding in the present work; namely, the frequency of the first burst band is tunable by changing the *i*-GaAs layer thickness d .

Next, we discuss the mechanism of the frequency shift of the first burst band. Since a decrease in the *i*-GaAs layer thickness leads to the enhancement of the built-in electric field as shown in Table 1, the high frequency shift of the first burst band indicates that the photo-generated carriers are monotonously accelerated by the built-in electric field. Thus, it is concluded that the intervalley scattering, which dominates the carrier-transport process under the steady state condition in a high electric field range, hardly influences in the sub-picosecond range. It should be noted that the frequency shift of the first burst band is not related to plasmons because the pump power was fixed to 40 mW in the present experiment.

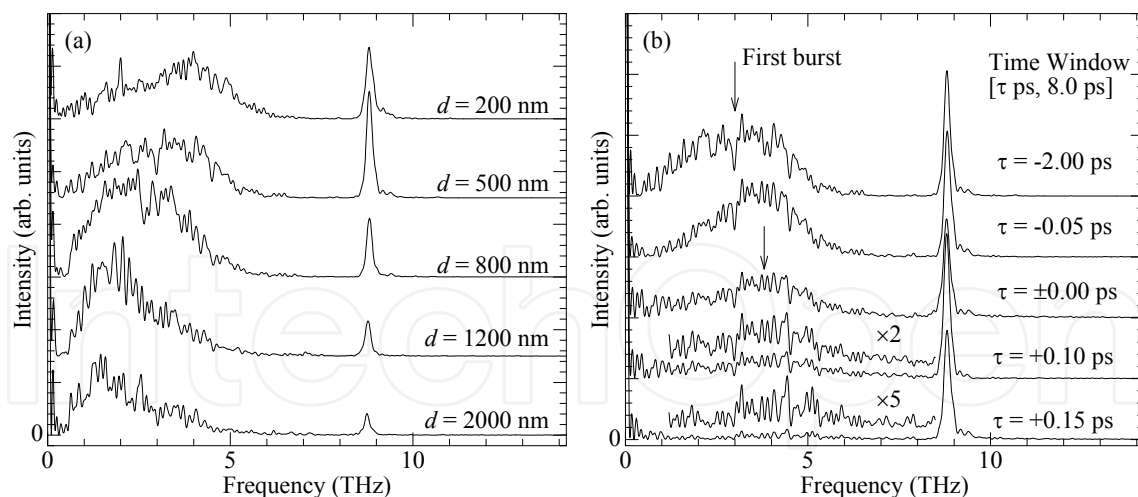


Fig. 10. (a) Fourier power spectra of the terahertz waveforms of the *i*-GaAs(*d* nm)/*n*-GaAs samples shown in Fig. 10(a). (b) Time-partitioning Fourier power spectra of the terahertz waveforms of the *i*-GaAs(500 nm)/*n*-GaAs sample. The values of τ are -2.00, ± 0.00 , +0.10 and +0.15 ps.

We also confirmed that the photogenerated carriers are monotonously accelerated by the built-in electric field, using a time-partitioning Fourier transform method, which is a powerful way to investigate the time evolution of the signal. The time-partitioning Fourier power spectrum $I(\omega)$, where ω is a frequency, is given by

$$I(\omega) \propto \left| \int_{\tau}^{8\text{ps}} A(t) \exp(-i\omega t) dt \right|^2. \quad (3)$$

Here, $A(t)$ is the time-domain terahertz waveform and τ is the time delay ($-2 \text{ ps} \leq \tau < 8 \text{ ps}$) that determines the time window of the Fourier transform.

Figure 10(b) shows the time-partitioning Fourier power spectra of the *i*-GaAs(500 nm)/*n*-GaAs sample at various time windows. The peak frequency of the first burst is shifted to the high frequency side with an increase in τ . In general, the frequency of the electromagnetic wave reflects with an increase in the electron velocity, which is the well-known fundamental concept on the high-frequency devices for microwave generation. Consequently, it is confirmed that the monotonous acceleration of the photogenerated carriers is responsible for the high frequency shift of the first burst band shown in Fig. 10(a).

It is interesting to compare the present results with those of the Monte Carlo simulation. According to the Monte Carlo simulation, the transient electron velocity in a GaAs crystal is accelerated by the electric field and reaches the maximum value of $5.5 \times 10^7 \text{ cm/s}$ at 0.5 ps in the condition of the electric field of 10 kV/cm. In the electric field of 20 kV/cm, the maximum transient electron velocity reaches $7 \times 10^7 \text{ cm/s}$ at 0.3 ps (Tomizawa, 1993). Taking account of the above-mentioned simulation, our experimental results are reasonable.

4.4 Intense terahertz emission from the coherent LO phonon

In advance to discuss the present results of the intense terahertz emission from the coherent LO phonon, we briefly describe the reason why it is desired to generate terahertz emission

from coherent LO phonons with use of simpler methods. The terahertz emission from coherent optical phonons has been attracting much attention since the development of monochromatic terahertz emitters is an important issue in terahertz-wave spectroscopy. In general, however, the intensity of the terahertz emission from coherent optical phonons is weak in bulk semiconductors (Gu & Tani, 2005). As a solution of this problem, the application of the multiple quantum wells was proposed (Mizoguchi et al., 2005; Nakayama et al., 2008; Nakayama & Mizoguchi, 2008). In the multiple quantum wells, the terahertz emission from the coherent LO phonon is enhanced in the case where the fundamental heavy-hole and light-hole exciton energy spacing is equal to the LO phonon frequency. In addition, the photon energy of the pump beam should be tuned to the center energy between the heavy-hole and light-hole exciton energy spacing: The quantum interference between the heavy-hole and light-hole excitons is a driving force for the coherent LO phonon. The above method requires the strict sample growth and limits the photon energy of the pump beam. In contrast to the former strategy for enhancing terahertz emission, the present strategy is quite simple. As mentioned in Subsection 4.3, the value of the photon energy of the pump beam is 1.57 eV, which is much higher than the fundamental transition energy of GaAs (1.424 eV) at room temperature, so that the excitation process by the pump beam is under the off-resonance condition. In addition, the sample structure consists of just two layers.

As shown in Fig. 10(a), the intensity of the LO phonon band increases with a decrease in d that enhances the built-in electric field of the i -GaAs layer. In $d = 500$ nm, the peak intensity of the LO phonon band exceeds that of the first burst band peaking at about 3.0 THz. It should be noted that, in the present experiment, the frequency-dependent sensitivity of the dipole antenna (the detector) was not calibrated. In general, the sensitivity of the dipole antenna remarkably lowers in a high frequency range. Actually, the sensitivity at 1 THz remarkably drops above 5.0 THz by the factor of 10^{-3} at least (Bolivar, 1999). The intensity of the coherent LO phonon band, therefore, has a possibility of drastically exceeding that of the first burst band. The present observation of the intense terahertz wave from the coherent LO phonons results from the following two factors. The one factor is the sweeping-out effects on carriers owing to the presence of the built-in electric field in the i -GaAs layer, which reduces the free-carrier absorption of the terahertz wave. The second factor is an increase in initial displacements of the constituent atoms. From the viewpoint of the polarization dynamics, we explain the generation mechanism of the terahertz wave from coherent LO phonon in detail together with its relation with initial displacements of the constituent atoms. As shown in Table 1, the increase in the built-in electric field enlarges the initial displacements of the constituent Ga and As atoms; namely, the static polarization due to the initial displacements is enhanced. The initial displacements are released by the instantaneous change in the built-in electric field by the surge current, which launches the coherent oscillation of the constituent atoms, i.e., the coherent LO phonon (Cho et al., 1990; Dekorsy et al., 2000). This phenomenon leads to the oscillation of the LO-phonon polarization producing the terahertz wave. It is noted that the enlargement of the initial displacement results in the enhancement of the amplitude of the coherent LO phonon. Consequently, taking account of the generation mechanism of the coherent LO phonon mentioned above, it is apparent that the terahertz-wave intensity from the coherent LO phonon is increased with a decrease in d .

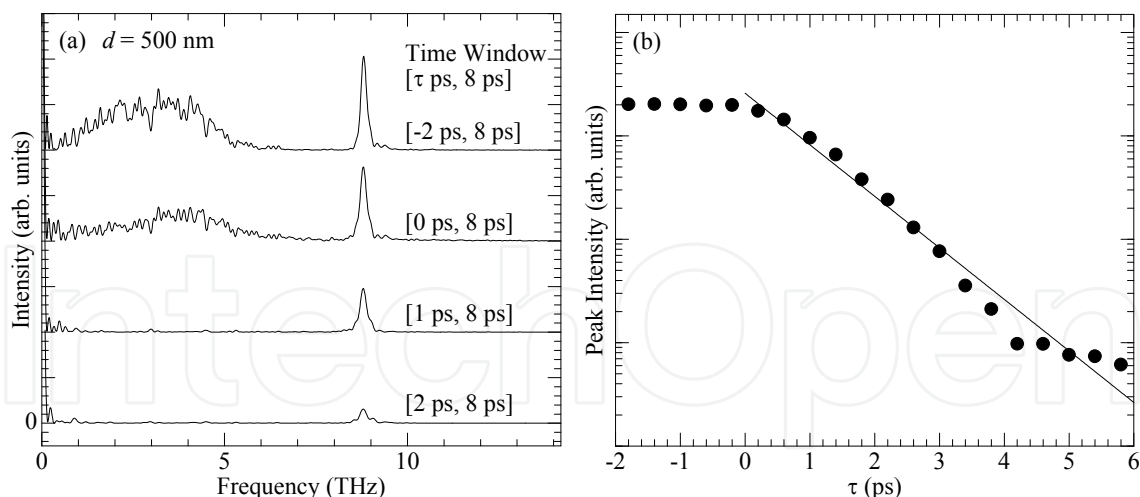


Fig. 11. (a) Time-partitioning Fourier power spectra of the terahertz waveforms of the *i*-GaAs(500 nm)/*n*-GaAs sample. The values of τ are -2, 0, 1 and 2 ps. (b) Peak intensities of the LO phonon bands of the *i*-GaAs(500 nm)/*n*-GaAs sample plotted as a function of τ . The solid line indicates the fitting results of a single exponential function.

In the *i*-GaAs(200 nm)/*n*-GaAs sample, the intensity of the coherent LO phonon band is slightly reduced though the built-in electric field is the highest in all the samples. The reduction of the intensity of the coherent LO phonon in the *i*-GaAs(200 nm)/*n*-GaAs sample in comparison with that in the *i*-GaAs(500 nm)/*n*-GaAs sample mainly results from the decrease of the *i*-GaAs layer thickness, i.e. the volume effect.

We also analyzed the time evolution of the terahertz wave from the coherent LO phonon with use of the time-partitioning Fourier transform method. Figure 11(a) shows the time-partitioning Fourier transform spectra of the *i*-GaAs(500 nm)/*n*-GaAs sample. The band of the first burst between 0 to 5 THz rapidly decays and disappears at $\tau = 1$ ps, which coincides with the fact that the first burst appears around the time delay of 0 ps in the terahertz waveform shown in Fig. 10(a). In contrast, the LO phonon band at 8.8 THz still remains at $\tau = 2$ ps, which is consistent with the fact that the oscillatory profile of the coherent LO phonon signals is observed up to 5 ps in the THz waveforms. The decay rate of the coherent LO phonon is estimated from Fig. 11(b) to be 1.1 ps^{-1} using a single exponential function fitting. As indicated in Eq. (3), the decay rate is estimated from the Fourier power spectrum that corresponds to the square of the amplitude. Consequently, the decay rate of the amplitude of the terahertz wave from the coherent LO phonon, which is shown in Fig. 9(a), is a half value of the decay rate estimated from the time-partitioning Fourier transform method. The decay rate is about 0.5 ps^{-1} , so that the decay time is 2.0 ps. Note that the decay time of terahertz wave from the coherent LO phonon is longer than that of the decay time of terahertz wave from the first burst. This is advantageous to control the mechanical delay line, the stepper, which is explained in Subsection 3.3.

The above-mentioned result opens the way to the novel terahertz-wave imaging system. In general, the spatial resolution of the terahertz-wave image is 1 mm at most (Herman et al., 2005). This fact originates from the diffraction limit of the terahertz wave emitted from the conventional dipole antenna. The dipole antenna emits a terahertz wave with a frequency range from 0 to 5 THz. The position of the peak intensity of the band locates at about 1.0 THz. This frequency corresponds to the wavelength λ of $300 \mu\text{m}$. In addition, the frequency

range of the terahertz wave from the dipole antenna is relatively wide (Bolivar, 1999; Sakai & Tani, 2005), which leads to the possibility of causing the chromatic aberration.

The schematic view of the imaging system that we propose is shown in Fig. 12. Figure 12 is similar to the conventional terahertz-wave-transmittance imaging system (Herman et al., 2005). In the conventional system, a mirror is equipped at the position of the *i*-GaAs/*n*-GaAs terahertz emitter in Fig. 12. The expanded pump beam is reflected by the mirror and the dipole antenna in front of the sample is illuminated by the reflected pump beam. The terahertz wave emitted from the dipole antenna is transmitted and detected with use of electro-optic crystals, for example, ZnTe. At each point of the crystal, the electric field of the terahertz wave modulates the refractive index through the electro-optic effects. This phenomenon modifies the polarization of the probe beam, and only the component of the probe beam with the modified polarization passes the analyzer. The charge-coupled-device (CCD) camera makes a terahertz-wave transmittance image by detecting these components. This is the so-called electro-optic sampling method, which is a well-established technique. The imaging system that we propose is based on the above-mentioned electro-optic sampling method. The difference is the position of the terahertz emitter, which is equipped instead of the mirror providing the expanded pump beam for the dipole antenna. In addition, the scan range, which is controlled by the delay line, is limited within the range that the terahertz wave from coherent LO phonon appears. The frequency of the GaAs LO phonon (8.8 THz) corresponds to the wavelength of 34 μm , which is much shorter than that of the terahertz wave from the dipole antenna (300 μm). Thus, the resolution of the image is improved by a factor of 10: the spatial resolution is estimated to be 0.1 mm. In the field of medical science, it was reported that the terahertz wave is sensitive to skin cancers (Wallace et al., 2004). Accordingly, the spatial resolution improvement contributes to the detection of the cancer at the earlier stage.

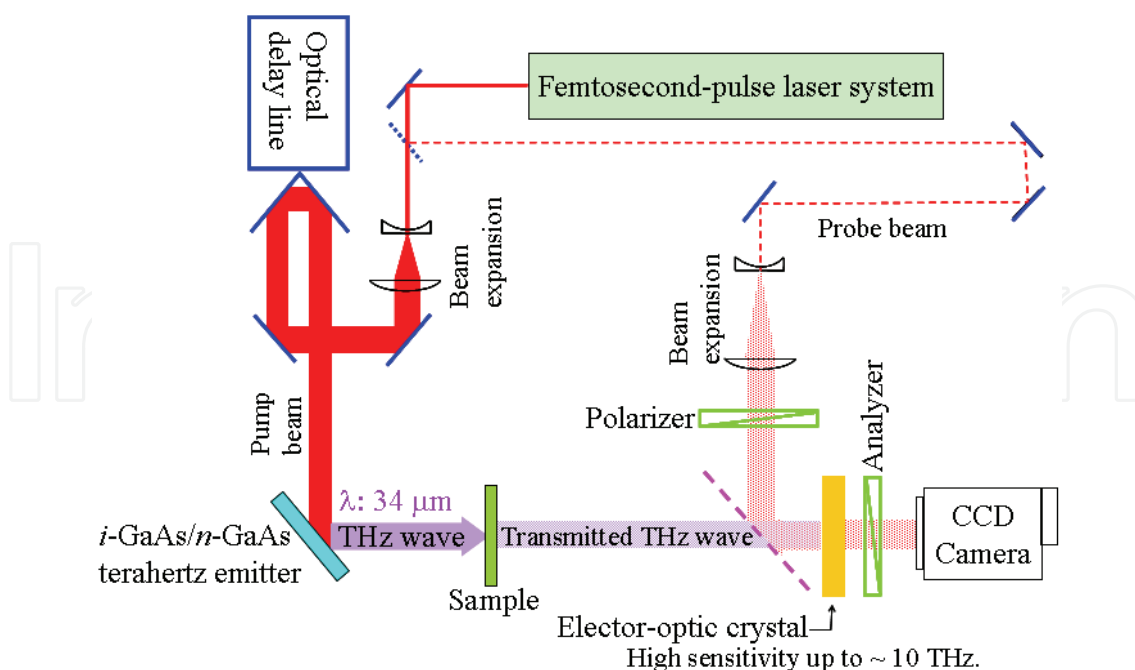


Fig. 12. Schematic view of the terahertz-wave-transmittance imaging system with use of the terahertz emission from the coherent LO phonon. The abbreviation “THz wave” corresponds to “terahertz wave”.

5. Analysis of the epitaxial layer structures emitting the terahertz wave: direction reversal of the surface band bending in GaAs-based dilute nitride epitaxial layers

5.1 Relation between the polarity of the terahertz wave and surface band bending

In Section 4, we describe the relation between the photogenerated carrier transport process and terahertz-wave frequency. The results of Section 4 indicate that the emitted terahertz wave itself contains a large amount of information on an epitaxial layer structure for its source. In Section 5, we focus our attention on the relation between the polarity of the terahertz wave and the surface band bending.

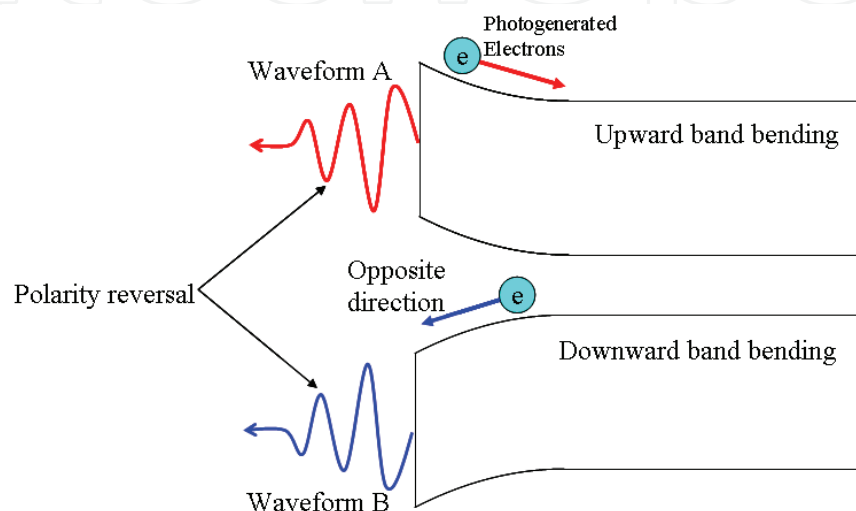


Fig. 13. Relation between the surface band bending and terahertz-wave polarity.

Figure 13 schematically shows the relation between the direction of the surge current and the surface band bending. According to Eq. (1), the electric field of the terahertz wave is proportional to the time derivative of the surge current. Equation (1) indicates that the polarity of the terahertz wave reflects the direction of the surge current. In the sample with the upward surface band bending, the photogenerated electrons flow into the inside of the crystal, and the terahertz wave is emitted with the waveform labeled by A. In contrast, in the sample with the downward band bending, the photogenerated electrons flow toward the surface, and the terahertz wave is emitted with the waveform labeled by B. Comparing the waveform A with the waveform B, it is apparent that the change in an electron-flow direction causes the reversal of the polarity of the terahertz wave; therefore, the terahertz-wave polarity is sensitive to the direction of the surface band bending.

5.2 Energy band structure of GaAs-based dilute nitrides

In this subsection, we briefly describe the reason why we focus our attention on the surface band bending of GaAs-based dilute nitrides. GaAs-based dilute nitrides, e.g. $\text{GaAs}_{1-x}\text{N}_x$ and $\text{In}_y\text{Ga}_{1-y}\text{As}_{1-x}\text{N}_x$, have an interesting property that they exhibit giant negative bowing of the band-gap energy as a function of nitrogen content. For example, in $\text{GaAs}_{1-x}\text{N}_x$, the reduction of the band-gap energy is estimated to be 180 meV per nitrogen mole fraction of 1% (Walukiewicz et al., 2008). The mechanism of the band-gap energy reduction has been intensively investigated. According to the earlier work in GaAs-based dilute nitrides (Shan

et al., 1999), a strong interaction between the conduction band of the host material and the nitrogen energy level causes a band anticrossing, which produces the lower and upper subbands. The lower subband corresponds to the band edge, and the band-gap energy exhibits a large negative bowing. Thus, the origin of the band-gap energy bowing has been identified.

It is considered that, like other compound semiconductors, the GaAs-based dilute nitride epitaxial layers also have a surface band bending, which is dominated by numerous deep levels on the surface. The above consideration gives rise to an interesting issue whether the incorporation of nitrogen modifies the surface band bending, which is the present motivation.

5.3 Samples and experimental procedures

The present samples were the undoped $\text{GaAs}_{1-x}\text{N}_x$ epitaxial layers with $x = 0.43\%$ and with $x = 1.53\%$, and an $\text{In}_y\text{Ga}_{1-y}\text{As}_{1-x}\text{N}_x$ epitaxial layer with $x = 5.0\%$ and $y = 14\%$ grown by metal organic vapour phase epitaxy. The thicknesses of the $\text{GaAs}_{1-x}\text{N}_x$ and $\text{In}_y\text{Ga}_{1-y}\text{As}_{1-x}\text{N}_x$ epitaxial layers were 500 nm. The $i\text{-GaAs}(200\text{ nm})/n\text{-GaAs}(3\text{ }\mu\text{m}, 3 \times 10^{18}\text{ cm}^{-3})$ structure was also used as a reference sample. This is because, as described in Sections 3 and 4, the potential structure of the $i\text{-GaAs}(200\text{ nm})/n\text{-GaAs}$ sample has a linear potential slope categorized into an upward surface band bending. We also used a CrO-doped semi-insulating GaAs bulk crystal as a sample to evaluate the effects of the incorporation of nitrogen.

The time-domain terahertz waves from the samples were measured at room temperature with use of laser pulses with a duration time of about 70 fs. The measurement system for the terahertz wave was the same shown in Fig. 5. The emitted terahertz beam was received by an optically gated bow-tie antenna with a gap of 5.0 μm formed on a low-temperature-grown GaAs. The power of the gate beam was fixed to 4.0 mW. A typical pump-beam power was 40 mW, and the wavelength was 800 nm. The phase of the lock-in amplifier was tuned with use of the signal of the $i\text{-GaAs}(200\text{ nm})/n\text{-GaAs}$ sample and was fixed in all measurements.

5.4 Polarity reversal and the origin of the modification of the surface band bending in GaAs-based diluten

Figure 14 shows the terahertz waveforms of the $i\text{-GaAs}(200\text{ nm})/n\text{-GaAs}$, semi-insulating GaAs, $\text{GaAs}_{1-x}\text{N}_x$, and $\text{In}_y\text{Ga}_{1-y}\text{As}_{1-x}\text{N}_x$ samples. All the samples show the first burst around the time delay of 0 ps. As the time delay increases, the polarity of the terahertz waveform changes from the negative to the positive in the $i\text{-GaAs}(200\text{ nm})/n\text{-GaAs}$ sample. The terahertz-waveform polarity of the semi-insulating GaAs sample is the same as that of the $i\text{-GaAs}(200\text{ nm})/n\text{-GaAs}$ sample, which indicates that the direction of the photogenerated current producing the terahertz wave is the same between the $i\text{-GaAs}(200\text{ nm})/n\text{-GaAs}$ and semi-insulating GaAs samples. Accordingly, it is considered that the present semi-insulating GaAs sample has an upward band bending at the surface region. As shown in Fig. 14, the amplitude of the first-burst of the semi-insulating GaAs sample is the smallest, which suggests that the surface band bending is relatively small.

In contrast, the terahertz-waveform polarities of the $\text{GaAs}_{1-x}\text{N}_x$ samples reverse in comparison with that of the $i\text{-GaAs}(200\text{ nm})/n\text{-GaAs}$ sample, which means that the surge current direction in the $\text{GaAs}_{1-x}\text{N}_x$ samples is opposite to that in the $i\text{-GaAs}(200\text{ nm})/n\text{-GaAs}$ sample. The $\text{GaAs}_{1-x}\text{N}_x$ samples, therefore, have a downward band bending at the surface

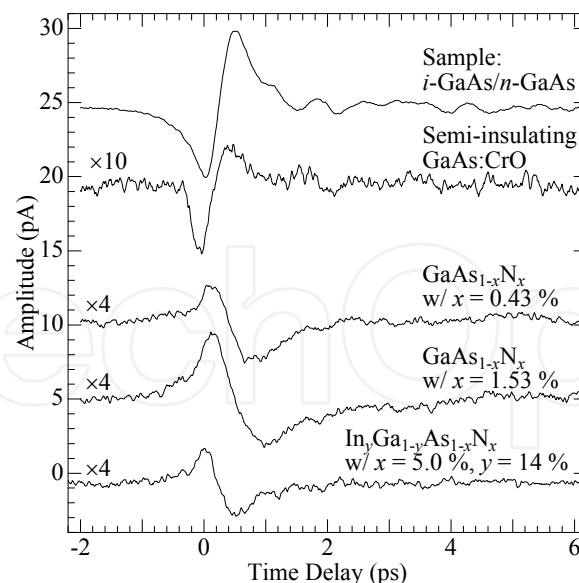


Fig. 14. Amplitudes of the terahertz waveforms of the *i*-GaAs(200 nm)/*n*-GaAs, semi-insulating GaAs, and GaAs_{1-x}N_x ($x = 0.43\%$ and 1.53%), and In_yGa_{1-y}As_{1-x}N_x samples as a function of time delay at room temperature. The pump-beam power was 40 mW.

region. It is noteworthy that, even in the GaAs_{1-x}N_x sample with $x = 0.43\%$, the polarity is inverted in comparison with that of the *i*-GaAs(200 nm)/*n*-GaAs sample. Comparing the polarity of the semi-insulating GaAs sample with the polarity of the GaAs_{1-x}N_x sample with $x = 0.43\%$, it is evident that the incorporation of the small amount of nitrogen changes the direction of the surface band bending. In addition, the amplitude of the GaAs_{1-x}N_x sample with $x = 1.53\%$ is larger than the amplitude of the GaAs_{1-x}N_x sample with $x = 0.43\%$, which indicates that, in the GaAs_{1-x}N_x samples, the magnitude of the downward band bending is enhanced with an increase in the incorporation of nitrogen. We also note that, in the In_yGa_{1-y}As_{1-x}N_x sample, the polarity reversal of the terahertz waveform is observed. It is, therefore, concluded that the direction reversal of the surface band bending induced by the incorporation of nitrogen is universal in GaAs-based dilute nitrides.

Next, we discuss the mechanism causing the reversal of the direction of the surface band bending in the GaAs_{1-x}N_x samples. In general, the surface Fermi level pinning originates from a large amount of deep levels at the surface locating within the forbidden band. The electronic wave functions of the deep levels are strongly localized in the atomic-order region. The average distance between the nitrogen atoms is estimated to be several ten nanometers in a GaAs_{1-x}N_x epitaxial layer with $x = 1\%$, taking account of the fact that the atomic monolayer thickness is 0.283 nm for the (001) direction in GaAs (Madelung, 2004). In addition, the energy of the nitrogen level locates above the conduction-band bottom. These facts suggest that the nitrogen incorporation can not disturb the electronic wave functions of the deep levels; therefore, the energies of the deep levels relative to the vacuum level are not influenced by the nitrogen incorporation.

The nitrogen incorporation, however, influences the conduction band according to the band anticrossing model. In the framework of this model, the conduction band of GaAs strongly interacts with the energy level of the incorporated nitrogen. As a result, the conduction band of GaAs splits into the upper (E_+) and lower (E_-) subbands, whose energies at Γ -point are expressed by the following equation (Walukiewicz et al., 2008):

$$E_{\pm} = \frac{1}{2} \left[(E_{g,\text{GaAs}} + E_N) \pm \sqrt{(E_{g,\text{GaAs}} - E_N)^2 + 4x C_{\text{GaAs},N}^2} \right]. \quad (4)$$

The quantities of $E_{g,\text{GaAs}}$, E_N , and $C_{\text{GaAs},N}$ are the fundamental transition energy of GaAs, the energy position of nitrogen-related level, and the hybridization matrix element, respectively (Walukiewicz et al., 2008). The energy level of the incorporated nitrogen locates above the conduction-band bottom by 226 meV, where the value of 226 meV corresponds to the energy difference between E_N and the conduction-band bottom of GaAs (Walukiewicz et al., 2008). The above interaction generates the E_+ and E_- subbands through the band anticrossing. We, for example, calculated the energies of the E_+ and E_- subbands in the $\text{GaAs}_{1-x}\text{N}_x$ sample with $x = 1.53\%$ using Eq. (4). In the calculation, the values of $E_{g,\text{GaAs}}$, E_N , and $C_{\text{GaAs},N}$ are 1.424 (Madelung, 2004), 1.65, and 2.7 eV (Walukiewicz et al., 2008), respectively. The E_- and E_+ subband energies at the Γ point are estimated to be 1.890 and 1.184 eV, respectively. This result indicates that the incorporation of the nitrogen lowers the energy of the conduction band bottom by 240 meV in the $\text{GaAs}_{1-x}\text{N}_x$ sample with $x = 1.53\%$. The bottom energy of the E_- subband relative to the vacuum level, therefore, becomes larger than the conduction bottom energy of GaAs relative to the vacuum level; namely, the E_- subband bottom approaches the deep levels responsible for the surface Fermi level pinning.

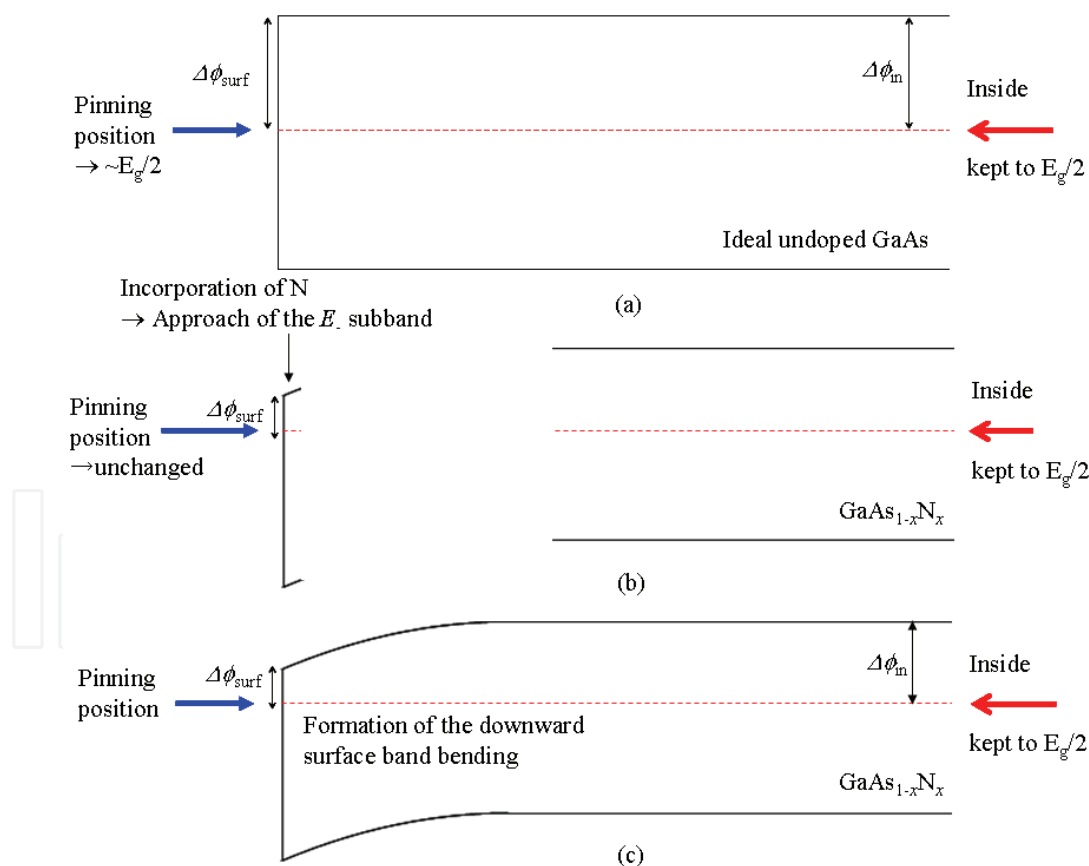


Fig. 15. Formation process of the downward surface band bending in $\text{GaAs}_{1-x}\text{N}_x$. (a) Before the incorporation of nitrogen. (b) Difference in the effects of the nitrogen incorporation between the inside and surface of the epitaxial layer. (c) Formation of the downward surface band bending.

In contrast, in the inside far away from the surface, the Fermi level in $\text{GaAs}_{1-x}\text{N}_x$ locates at almost the center of the band gap according to thermal statistical mechanics.

Here, using Fig. 15, we discuss the process the formation of the downward surface band bending in $\text{GaAs}_{1-x}\text{N}_x$. We denote the difference in energy between the conduction-band bottom and the surface Fermi level as $\Delta\phi_{\text{surf}}$. Figure 15(a) shows the band structure of ideal undoped GaAs. In the case where the nitrogen incorporation causes the downward shift of the E_c subband, the quantity of $\Delta\phi_{\text{surf}}$ becomes smaller, as shown in Fig. 15(b). In the same manner, we denote the energy difference between the conduction-band bottom and the Fermi level in the inside of the crystal as $\Delta\phi_{\text{in}}$. From the above discussion on the Fermi level in the inside of the crystal, it is apparent that $\Delta\phi_{\text{in}}$ is constant and that the value of $\Delta\phi_{\text{in}}$ is almost equal to the half of the band-gap energy. Thermal statistical mechanics tells us that, at equilibrium, the Fermi level is uniform from the surface to the inside in the crystal. It should be reminded that the surface Fermi level locates at the center of the band gap in GaAs, which means that the surface band bending is negligibly small in the ideal GaAs crystal (Fig. 15(a)): $\Delta\phi_{\text{surf}} - \Delta\phi_{\text{in}} \approx 0$. In $\text{GaAs}_{1-x}\text{N}_x$, even the small nitrogen incorporation makes the value of $\Delta\phi_{\text{surf}} - \Delta\phi_{\text{in}}$ negative owing to the band anticrossing producing E_c subband in the conduction band, which bends the conduction band downward as shown in Fig 15(c). Thus, it is concluded that the downward surface band bending in the $\text{GaAs}_{1-x}\text{N}_x$ epitaxial layer results from the shift of the E_c subband toward the surface Fermi level at the surface region. This is the origin of the polarity reversal of the terahertz waveform.

5.5 Precise evaluation of the $\text{GaAs}_{1-x}\text{N}_x$ epitaxial layer with use of the combination of the photoreflectance and terahertz-wave measurements

In Subsection 5.4, we demonstrate that the terahertz-wave measurement is applicable to the investigation of the surface band bending. As described in Section 4, the photoreflectance spectroscopic measurement is useful to estimate the built-in electric field, though this measurement provides only the electric field *strength*. Accordingly, the combination of the photoreflectance and terahertz-wave measurements has the ability to precisely evaluate the surface band bending.

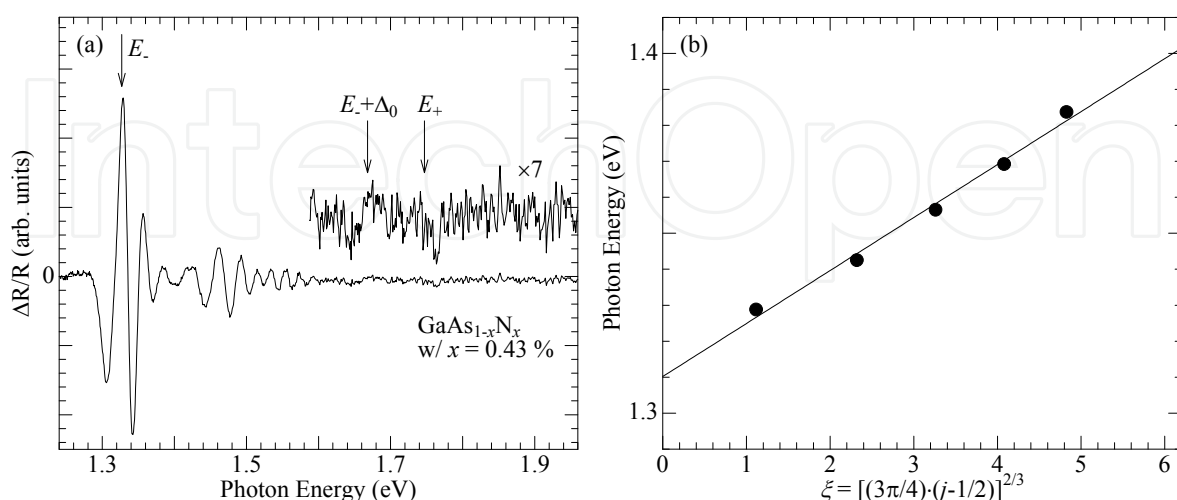


Fig. 16. (a) Photoreflectance spectrum of the $\text{GaAs}_{1-x}\text{N}_x$ sample with $x = 0.43\%$ at room temperature. (b) Linear plot of the extrema of the FKO's from the $\text{GaAs}_{1-x}\text{N}_x$ sample with $x = 0.43\%$ as a function of the quasi-index ξ .

Figure 16(a) shows the photoreflectance spectrum of the $\text{GaAs}_{1-x}\text{N}_x$ sample with $x = 0.43\%$. The position of the arrow labeled E_- at 1.327 eV (E_+ at 1.747 eV) corresponds to the energy of the transition between the lower (upper) conduction subband and heavy hole and/or light hole bands at the Γ -point, and the position of the arrow labeled $E_+ + \Delta_0$ at 1.668 eV corresponds to the E_- -subband-split-off-hole-band transition at the Γ -point, where the energies of E_- , E_+ , and $E_+ + \Delta_0$ are calculated on the basis of the band anticrossing model (Walukiewicz et al., 2008). Consequently, the oscillation pattern starting from about 1.3 eV is assigned to the FKO from the $\text{GaAs}_{1-x}\text{N}_x$ layer, while the oscillation pattern starting from about 1.4 eV is assigned to the FKO from the GaAs buffer layer. In order to estimate the surface electric field, as shown in Fig. 16(b), the extrema of the FKOs from the $\text{GaAs}_{1-x}\text{N}_x$ sample with $x = 0.43\%$ are plotted as a function of the quasi-index ξ . In the same manner applied in Section 4, the surface electric field is estimated to be 24 kV/cm using an interband reduced mass of $0.0689m_0$ (Walukiewicz et al., 2008). In general, undoped GaAs crystals have a surface electric field of several kV/cm at most. The present results indicate that the nitrogen incorporation enhances the surface electric field.

6. Conclusion

In the present chapter, we have described the terahertz electromagnetic wave from semiconductor epitaxial layer structures. In Section 2, we have pointed out the problems in photoconductive-antenna-based terahertz emitters. In Sections 3 and 4, we have focused our attention on the $i\text{-GaAs}(d \text{ nm})/n\text{-GaAs}(3 \mu\text{m}, 3 \times 10^{18} \text{ cm}^{-3})$ epitaxial layer structures. It has been clarified that the appropriate design of the epitaxial layer, which is based on semiconductor physics, is effective to control the characteristics of the terahertz wave: the emission intensity and frequency. In addition, we have elucidated the photogenerated carrier transport process in the sub-picosecond range. Furthermore, we have demonstrated the relatively intense terahertz emission from the coherent LO phonon and have proposed an example of its application. In Section 5, we have indicated that the terahertz wave contains the information of its source materials. From the polarity reversal of the terahertz waveform, it has been clarified that the GaAs-based dilute nitride ($\text{GaAs}_{1-x}\text{N}_x$ and $\text{In}_y\text{Ga}_{1-y}\text{As}_{1-x}\text{N}_x$) epitaxial layers have a downward band bending owing to the band anticrossing induced by the nitrogen incorporation. This finding suggests that the terahertz wave has the ability not only to probe the samples under test but also to reveal the physical properties of the materials emitting the terahertz wave.

The present approach to the terahertz wave is quite different from the approach used in the research field of microwaves because antenna structures are out of the scope. This is because the terahertz waves have a frequency range between infrared light and microwaves; namely, the terahertz waves have the properties both of light and of microwaves. However, on the basis of Faraday's law of induction, the generation mechanism of the terahertz wave is the same as that of the microwave. In fact, the terahertz wave from the coherent LO phonon is categorized into the typical dipole radiation. Accordingly, we conclude that the progress in the terahertz-wave technology depends on the fusion of the conventional concepts in the research fields of optics and of microwaves.

In the present chapter, we have focused our attention on the terahertz emitters. It is also important to precisely investigate the detection mechanism/method of the terahertz wave. To finalize the present chapter, we point out the above-mentioned issue.

7. Acknowledgements

The author acknowledges Professor Masaaki Nakayama, Mr. Syuichi Tsuruta (Osaka City University), and Dr. Takayuki Hasegawa (Hyogo Prefecture University) for their aid and useful discussion. The author also appreciates Dr. Hisashi Yamada and Dr. Masahiko Hata (Tsukuba Research Laboratory, Sumitomo Chemical Co., Ltd.) for the growth of the *i*-GaAs/*n*-GaAs structures. The GaAs_{1-x}N_x and In_yGa_{1-y}As_{1-x}N_x epitaxial layers were provided from Sumitomo Electric Industries. The present work is partially supported by Grant-in-Aid for Young Scientists (B) No. 22760010 from Japan Society for the Promotion of Science.

8. References

8.1 Journal papers

- Abe, H.; Harima, H.; Nakashima, S.; Tani, M.; Sakai, K.; Tokuda, Y.; Kanamoto, K. & Abe, Y. (1996). Characterization of Crystallinity in Low-Temperature-Grown GaAs Layers by Raman Scattering and Time-Resolved Photoreflectance Measurements, *Japanese Journal of Applied Physics*, Vol. 35, Part 1, No. 12A, pp. 5955-5963, ISSN: 00214922.
- Aspnes, D. E. (1974). Band nonparabolicities, broadening, and internal field distributions: The spectroscopy of Franz-Keldysh oscillations, *Physical Review B*, Vol. 10, Issue 10, pp. 4228-4238, ISSN: 10980102.
- Aspnes, D. E. (1983). Recombination at semiconductor surfaces and interfaces, *Surface Science*, Vol. 132, Issue 1-3, pp. 406-421, ISSN: 00396028.
- Auston, D. H. (1975). Picosecond optoelectronic switching and gating in silicon, *Applied Physics Letters*, Vol. 26, Issue 3, pp. 101-103, ISSN: 00036951.
- Basore, P. A. (1990). Numerical modeling of textured silicon solar cells using PC-1D, *IEEE Transaction on Electron Devices*, Vol. 37, No. 2, pp. 337-343, ISSN: 00189383.
- Blakemore, J. S. (1982). Semiconducting and other major properties of gallium arsenide, *Journal of Applied Physics*, Vol. 53, Issue 10, pp. R123-R181, ISSN: 00218979.
- Cho, G. C.; Kütt, W. & Kurz, H. (1990). Subpicosecond Time-Resolved Coherent-Phonon Oscillations in GaAs, *Physical Review Letters*, Vol. 65, Issue 6, pp. 764-766, ISSN: 00319007.
- Gupta, S.; Frankel, M. Y.; Valdmanis, J. A.; Whitaker, J. F.; Mourou, G. A.; Smith, F. W. & Calawa, A. R. (1991). Subpicosecond carrier lifetime in GaAs grown by molecular beam epitaxy at low temperatures, *Applied Physics Letters*, Vol. 59, Issue 25, pp. 3276-3278, ISSN: 0036951.
- Heyman, J. N.; Coates, N.; Reinhardt, A. & Strasser, G. (2003). Diffusion and drift in terahertz emission at GaAs surfaces, *Applied Physics Letters*, Vol. 83, Issue 26, pp. 5476-5478, ISSN: 0036951.
- Hu, B. B. & Nuss, M. C. (1995). Imaging with terahertz waves, *Optics Letters*, Vol. 20, Issue 16, pp. 1716-1718, ISSN: 01469592.
- Huang, H. C.; Yee, S. & Soma, M. (1990). The carrier effects on the change of the refractive index for *n*-type GaAs at $\lambda = 1.06, 1.3$, and $1.55 \mu\text{m}$, *Journal of Applied Physics*, Vol. 67, Issue 3, pp. 1497-1503, ISSN: 00218979.
- Mizoguchi, K.; Furuichi, T.; Kojima, O.; Nakayama, M.; Saito, S.; Syouji, A. & Sakai, K. (2005). Intense terahertz radiation from longitudinal optical phonons in GaAs/AlAs multiple quantum wells, *Applied Physics Letters*, Vol. 87, Issue 9, pp. 093102 1-3, ISSN: 0036951.

- Nakayama, M.; Ito, S.; Mizoguchi, K.; Saito, S. and Sakai, K. (2008). Generation of Intense and Monochromatic Terahertz Radiation from Coherent Longitudinal Optical Phonons in GaAs/AlAs Multiple Quantum Wells at Room Temperature, *Applied Physics Express*, Vol. 1, No. 1, pp. 012004 1-3, ISSN: 18829778.
- Nakayama, M. & Mizoguchi, K. (2008). Interactions between coherent optical phonons and excitonic quantum beats in GaAs/AlAs multiple quantum wells: strategy for enhancement of terahertz radiation from coherent optical phonons, *Physica Status Solidi C*, Vol. 5, Issue 9, pp. 2911-2916, ISSN: 16101634.
- Nelson, F. R.; Miller, C.; Tu, C. W. & Sputz, S. K. (1987). Exciton binding energies from an envelope-function analysis of data on narrow quantum wells of integral monolayer widths in $\text{Al}_{0.4}\text{Ga}_{0.6}\text{As}/\text{GaAs}$, *Physical Review B*, Vol. 36, Issue 15, pp. 8063-8070, ISSN: 10980102.
- Othonos, A. (1998). Probing ultrafast carriers and phonon dynamics in semiconductors, *Journal of Applied Physics*, Vol. 83, Issue 4, pp. 1789-1830, ISSN: 00218979.
- Pollak, F. H. & Shen, H. (1993). Modulation spectroscopy of semiconductors: bulk/thin film, microstructures, surfaces/interfaces and devices, *Materials Science and Engineering R*, Vol. 10, Issue 7-8, pp. 275-374, ISSN: 0927796X.
- Sarukura, N.; Ohtake, H.; Izumida, S. & Liu, Z. (1998). High average-power THz radiation from femtosecond laser-irradiated InAs in a magnetic field and its elliptical polarization characteristics, *Journal of Applied Physics*, Vol. 84, Issue 1, pp. 654-656, ISSN: 00218979.
- Shan, W.; Walukiewics, W.; Ager, J. W., III; Haller, E. E.; Geisz, J. F.; Friedman, D. J.; Olson, J. M. & Kurz, S. R. (1999). Band Anticrossing in GaInNAs Alloys, *Physical Review Letters*, Vol. 82, Issue 6, pp. 1221-1224, ISSN: 00319007.
- Shen, H.; Dutta, M.; Fotiadis L.; Newman, P. G.; Moerkirk, R. P.; Chang, W. H. & Sacks, R. N. (1990). Photoreflectance study of surface Fermi Level in GaAs and GaAlAs, *Applied Physics Letters*, Vol. 57, Issue 20, pp. 2118-2120, ISSN: 0036951.
- Takeuchi, H.; Kamo, Y.; Yamamoto, Y.; Oku, T.; Totsuka, M. & Nakayama, M. (2005). Photovoltaic effects on Franz-Keldysh oscillations in photoreflectance spectra: Application to determination of surface Fermi level and surface recombination velocity in undoped GaAs/*n*-type GaAs epitaxial layer structures, *Journal of Applied Physics*, Vol. 97, Issue 6, pp. 093539 1-16, ISSN: 00218979.
- Takeuchi, H.; Yanagisawa, J.; Hasegawa, T. & Nakayama, M. (2008). Enhancement of terahertz electromagnetic wave emission from an undoped GaAs/*n*-type GaAs epitaxial layer structure, *Applied Physics Letters*, Vol. 93, Issue 8, pp. 081916 1-3, ISSN: 0036951.
- Takeuchi, H.; Yanagisawa, J.; Hashimoto, J. & Nakayama, M. (2009). Effects of nitrogen incorporation on a direction of a surface band bending investigated by polarity of terahertz electromagnetic waves in $\text{GaAs}_{1-x}\text{N}_x$ epitaxial layers, *Journal of Applied Physics*, Vol. 105, Issue 9, pp. 093539 1-4, ISSN: 00218979.
- Takeuchi, H.; Yanagisawa, J.; Tsuruta, S.; Yamada, H.; Hata, M. & Nakayama, M. (2010). Frequency Shift of Terahertz Electromagnetic Waves Originating from Sub-Picosecond-Range Carrier Transport in Undoped GaAs/*n*-type GaAs Epitaxial Layer Structures, *Japanese Journal of Applied Physics*, Vol. 49, No. 8, pp. 082001 1-5, ISSN: 00214922.

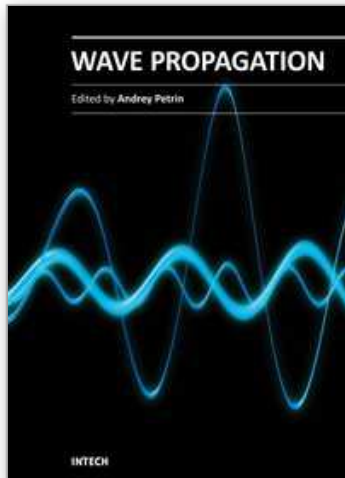
- Wallace, V. P.; Fitzgerald, A. J.; Shankar, S.; Flanagan, N.; Pye, R.; Cluff, J. & Arnone D. D. (2004). Terahertz pulsed imaging of basal cell carcinoma *ex vivo* and *in vivo*, *British Journal of Dermatology*, Vol. 151, Issue 2, pp. 424-432, ISSN: 00070963.
- Wieder, H. H. (1983). Surface Fermi level of III-V compound semiconductor-dielectric interfaces, *Surface Science*, Vol. 132, Issue 1-3, pp. 390-405, ISSN: 00396028.
- Yamamoto, K.; Yamaguchi, M.; Miyamaru, F.; Tani, M.; Hangyo, M.; Ikeda, T.; Matsushita, A.; Koide, K.; Tatsuno, M. & Minami, Y. (2004). Noninvasive Inspection of C-4 Explosive in Mails by Terahertz Time-Domain Spectroscopy, *Japanese Journal of Applied Physics*, Vol. 43, No. 3B, pp. L414 -L417, ISSN: 00214922.

8.2 Conference papers

- Clugston, D. A. & Basore P. A. (1998). PC1D VERSION 5: 32-BIT SOLAR CELL MODELING ON PERSONAL COMPUTERS, *Conference Record of the 26th IEEE Photovoltaic Specialists Conference*, pp. 207-210, ISBN: 0780337670, Anaheim, CA, U.S.A., September 1997, IEEE, Piscataway, NJ.

8.3 Books and book chapters

- Bolivar, P. H. (1999). Coherent terahertz spectroscopy, In: *SEMICONDUCTOR QUANTUM OPOELECTRONICS*, Millar, A.; Ebrahimzadeh, M & Finlayson, D. M. (Eds.), pp. 151-192, Institute of Physics, ISBN: 0750306297, Bristol.
- Dekorsy, T.; Cho, G. C. & Kurtz, H. (2000). Coherent Phonons in Condensed Media, In: *Light Scattering in Solids VIII*, Cardona, M. & Güntherodt, G (Eds.), pp. 169-209, Springer, ISBN: 3540660852, Berlin.
- Gu, P. & Tani, M. (2005). Terahertz Radiation from Semiconductor Surface, In: *Terahertz Optoelectronics*, Sakai, K. (Ed.), pp. 63-97, Springer, ISBN: 3540200130, Berlin.
- Herman, M.; Fukasawa, R. & Morikawa, O. (2005). Terahertz Imaging, In: *Terahertz Optoelectronics*, Sakai, K. (Ed.), pp. 203-270, Springer, ISBN: 3540200130, Berlin.
- Madelung, O. (2004). *Semiconductors -Basic Data (2nd ed.)*, Springer, ISBN: 3540608834, Berlin.
- Nishizawa, S.; Sakai, K.; Hangyo, M.; Nagashima, T.; Wada, M.; Tominaga, K.; Oka, A; Tanaka, K. & Morikawa, O. (2005). Terahertz Time-Domain Spectroscopy, In: *Terahertz Optoelectronics*, Sakai, K. (Ed.), pp. 203-270, Springer, ISBN: 3540200130, Berlin.
- Nuss, M. C. & Orenstein, J. (1999). Terahertz Time-Domain Spectroscopy, In: *Millimeter and Submillimeter Wave Spectroscopy of Solids*, Grüner, G. (Ed.), pp. 7-50, Springer, ISBN: 3540628606, Berlin.
- Ohtake, H.; Ono, S. & Sarukura, N. (2005). Enhanced Generation of Terahertz Radiation from Semiconductor Surface with External Magnetic Field, In: *Terahertz Optoelectronics*, Sakai, K. (Ed.), pp. 99-116, Springer, ISBN: 3540200130, Berlin.
- Sakai, K. & Tani, M. (2005). Introduction to Terahertz Pulse, In: *Terahertz Optoelectronics*, Sakai, K. (Ed.), pp. 1-30, Springer, ISBN: 3540200130, Berlin.
- Tomizawa, K. (1993). *Numerical Simulation of Submicron Semiconductor Devices*, Artech House, ISBN: 0890066205, Boston.
- Walukiewicz, W.; Alberi, K.; Wu, J.; Shan, W.; Yu, K. M. & Ager, J. W., III. (2008). Electronic Band Structure of Highly Mismatched Semiconductor Alloys, In: *Dilute III-V Nitride Semiconductors and Material Systems*, Erol, A. (Ed.), pp. 65-89, Springer, ISBN: 9783540745280, Berlin.



Wave Propagation

Edited by Dr. Andrey Petrin

ISBN 978-953-307-275-3

Hard cover, 570 pages

Publisher InTech

Published online 16, March, 2011

Published in print edition March, 2011

The book collects original and innovative research studies of the experienced and actively working scientists in the field of wave propagation which produced new methods in this area of research and obtained new and important results. Every chapter of this book is the result of the authors achieved in the particular field of research. The themes of the studies vary from investigation on modern applications such as metamaterials, photonic crystals and nanofocusing of light to the traditional engineering applications of electrodynamics such as antennas, waveguides and radar investigations.

How to reference

In order to correctly reference this scholarly work, feel free to copy and paste the following:

Hideo Takeuchi (2011). Terahertz Electromagnetic Waves from Semiconductor Epitaxial Layer Structures: Small Energy Phenomena with a Large Amount of Information, Wave Propagation, Dr. Andrey Petrin (Ed.), ISBN: 978-953-307-275-3, InTech, Available from: <http://www.intechopen.com/books/wave-propagation/terahertz-electromagnetic-waves-from-semiconductor-epitaxial-layer-structures-small-energy-phenomena>

INTECH
open science | open minds

InTech Europe

University Campus STeP Ri
Slavka Krautzeka 83/A
51000 Rijeka, Croatia
Phone: +385 (51) 770 447
Fax: +385 (51) 686 166
www.intechopen.com

InTech China

Unit 405, Office Block, Hotel Equatorial Shanghai
No.65, Yan An Road (West), Shanghai, 200040, China
中国上海市延安西路65号上海国际贵都大饭店办公楼405单元
Phone: +86-21-62489820
Fax: +86-21-62489821

© 2011 The Author(s). Licensee IntechOpen. This chapter is distributed under the terms of the [Creative Commons Attribution-NonCommercial-ShareAlike-3.0 License](https://creativecommons.org/licenses/by-nc-sa/3.0/), which permits use, distribution and reproduction for non-commercial purposes, provided the original is properly cited and derivative works building on this content are distributed under the same license.

IntechOpen

IntechOpen